Journal Pre-proof

Seismotectonic Analysis of the 2017 Moiyabana Earthquake (M_W6.5; Botswana), Insights from field investigations, aftershock and InSAR studies

T. Mulabisana, M. Meghraoui, V. Midzi, M. Saleh, O. Ntibinyane, T. Kwadiba, B. Manzunzu, O. Seiphemo, T. Pule, I. Saunders

PII: S1464-343X(21)00198-9

DOI: https://doi.org/10.1016/j.jafrearsci.2021.104297

Reference: AES 104297

To appear in: *Journal of African Earth Sciences*

Received Date: 8 April 2021

Revised Date: 3 June 2021

Accepted Date: 3 June 2021

Seismotectonic Analysis of the 2017 Moiyabana Earthquake

(M_W 6.5; Botswana),

Insights from field investigations, aftershock and InSAR studies

Mulabisana, T. [1, 2,5], Meghraoui, M.[1], Midzi, V.[2], Saleh, M.[1,3], Ntibinyane O. [4]

Kwadiba T.[4], Manzunzu, B. [2], Seiphemo O., Pule T.[2], Saunders I.[2]

[1] EOST- ITES, CNRS-UMR 7063, University of Strasbourg, France

[2] Council for Geoscience, 280 Pretoria Street, Silverton, Pretoria, South Africa

[3] NRIAG, Helwan, Egypt

[4] Botswana Geoscience Institute, Lobatse, Botswana

[5] Nelson Mandela University, Port Elizabeth, South Africa

07th April 2021

Seismotectonic Analysis of the 2017 Moiyabana Earthquake (M_W 6.5; Botswana), Insights from field investigations, aftershock and InSAR studies

Mulabisana, T. [1, 2,5], Meghraoui, M.[1], Midzi, V.[2], Saleh, M.[1,3], Ntibinyane O. [4]
Kwadiba T.[4], Manzunzu, B. [2], Seiphemo O. [4], Pule T.[2], Saunders I.[2]

[1] EOST- ITES, CNRS-UMR 7063, University of Strasbourg, France
[2] Council for Geoscience, 280 Pretoria Street, Silverton, Pretoria, South Africa
[3] NRIAG, Helwan, Egypt
[4] Botswana Geoscience Institute, Lobatse, Botswana
[5] Nelson Mandela University, Port Elizabeth, South Africa

3rd June 2021

Abstract

The 3 April 2017 M_W 6.5, Moiyabana (Botswana) earthquake occurred in the continental interior of the Nubian plate and in a seismogenic region previously considered as stable. Our objective is to combine several approaches (field and remote sensing investigations) in order to adopt a multidisciplinary strategy so as to enhance our understanding of earthquake occurrence in intraplate southern Africa. We analyse the mainshock and aftershocks sequence based on a local seismic network and local seismotectonic characteristics. The earthquake rupture geometry is constrained with more than 900 aftershocks recorded over a period of three months and from the InSAR analysis of Sentinel-1 images (ascending orbit). The mainshock (25.134 E, 22.565 S; depth 22 ± 3 km) was followed by more than 500 events of magnitude $M \geq 0.8$ recorded in April 2017 including the largest aftershock (M_W 4.6 on the 5 April 2017). Focal mechanism solutions of the mainshock and aftershocks display predominance of NW-SE trending and NE dipping normal faulting. Stress inversion of the focal mechanisms produced results that are compatible with a NE-SW extension under normal faulting regime. The InSAR study shows fringes (a pair of ascending images 2017-03-30 and 2017-04-11) with two lobes with 3.86 cm to 5.15 cm coseismic slip on a NW-SE elongated and 40-km-long surface deformation consistent with the mainshock location and normal faulting mechanism. The modelling of surface deformation provides the earthquake rupture dimension at depth with ~ 50 cm maximum slip on a fault plane striking 315°, dipping 45°, -80° rake and with M_o 3.68 x 10^{18} Nm. Although the seismic strain rate is of low level, the occurrence of the 2017 Moiyabana earthquake, followed by an aftershock sequence in the central Limpopo Mobile Belt classifies the intraplate region as an active plate interior.

Keywords: Seismotectonics, Earthquake, Fault, deformation, mainshock, aftershock

1 Introduction

Continental interiors are often considered as regions of low level of major earthquakes mostly because their earthquake catalogue is limited in time. Amid continental domains, intraplate southern Africa is classified as a Stable Continental Region (SCR) where the build-up of tectonic stresses is slow (e.g., < 8 nanostrain/yr.) and hence considered as among the Earth's least seismic active regions (Stamps et al., 2014; Njoroge et al., 2015; Saria et al., 2014; Johnston, 1996a, 1996b). Although the tectonic and seismicity strain rates are rather low (about 1 nanostrain/yr.) in intraplate southern Africa (the seismotectonic characteristics at the continental scale reveal the existence of active zones crossing the presumably stable African shields (Fig. 1; Hartnady, 1990; Meghraoui et al., 2016). Large earthquakes do occur in areas with no known major historical earthquakes, surface deformation or strain accumulation, but their sources are poorly known. The short record of instrumental and/or historical seismicity of these regions may preclude the full understanding of their seismogenic characteristics and occurrence rate of large earthquakes.

The 3 April 2017 Moiyabana earthquake with magnitude M_W 6.5 (Fig. 1) occurred in south-east Botswana, a region which is perceived as a stable continental tectonic domain with apparently no significant evidence of seismic strain release (Fig. 1). The main shock (25.134° E, 22.565° S, 26.5 ± 2.5 km depth according to the Council for Geoscience (CGS), Pretoria; Table 1) and aftershocks are located in a sparsely populated national park. Although the earthquake was widely felt in Botswana, South Africa and Zimbabwe, no severe damage was observed due to the low population density in the epicentral area (Midzi *et al.*, 2018). However, field investigations report slight structural damage with intensity of VI on the Modified Mercalli Intensity scale (MMI-56) observed at about 14 km, 40 km (in a mine) and 90 km mainly west of the epicentral location. In addition, Midzi *et al.* (2018) observed N-S trending clusters of aftershocks recorded during the first month with a spatial and temporal southward migration of seismic events. No strong seismic events have been reported in close proximity to the 2017 Moiyabana earthquake area, except for the 1952 Okavango and 2006 Machaze earthquakes (M_L6.7 and M_W7.0, respectively)

Studies on the earthquake activity of continental interiors have been mainly developed in the eastern United States and the New Madrid seismic zone (Hough and Page, 2011; Calais *et al*., 2016), in eastern Canada (Bent, 1994), in Central Europe (Camelbeeck and Meghraoui, 1998), in intraplate India (Rajendran *et al.*, 1996), in Mongolia (Chéry *et al*., 2001), and in Australia (Crone *et al.*, 1997; Clark *et al.*, 2008). Intraplate deformation can be assessed by the occurrence of strong earthquakes and identification of active tectonic structures in regions far from plate boundaries. The rigidity and stability of the southern Africa shield is questioned following the inferences from seismotectonic and geodetic studies that advocate the existence of incipient rifting south and southwest of the continental East African Rift (Fairhead and Henderson, 1977; Hartnady, 1990; Daly et al., 2020). Although GPS velocities are significantly lower than 1 mm/yr., (Fig. 1; Malservisi *et al.*, 2013; Saria *et al.,* 2014), different authors suggest that there might be a link between the 2017 Moiyabana earthquake sequence and the EARS (Fadel *et al.*, 2020; Chisenga et al., 2020). The invoked reasons are mainly the similarity between the normal faulting mechanism and related extensional tectonic stresses (Fadel *et al.,* 2020), the normal faulting activity of the EARS (e.g., the 22 February 2006 M_W 7.0 Machaze earthquake; Fenton and Bommer, 2006; Saunders et al., 2010) and the Okavango rift basin (e.g., the 11 October 1952 M_W 6.7 earthquake; Modisi *et al.*, 2000; Midzi *et al.,* 2018). Materna *et al.* (2019) imply that the occurrence of the 2017 event on the ancient tectonic zone of the Limpopo Mobile Belt may be responding to the stress field imposed by the EARS (Stamps et al, 2014).

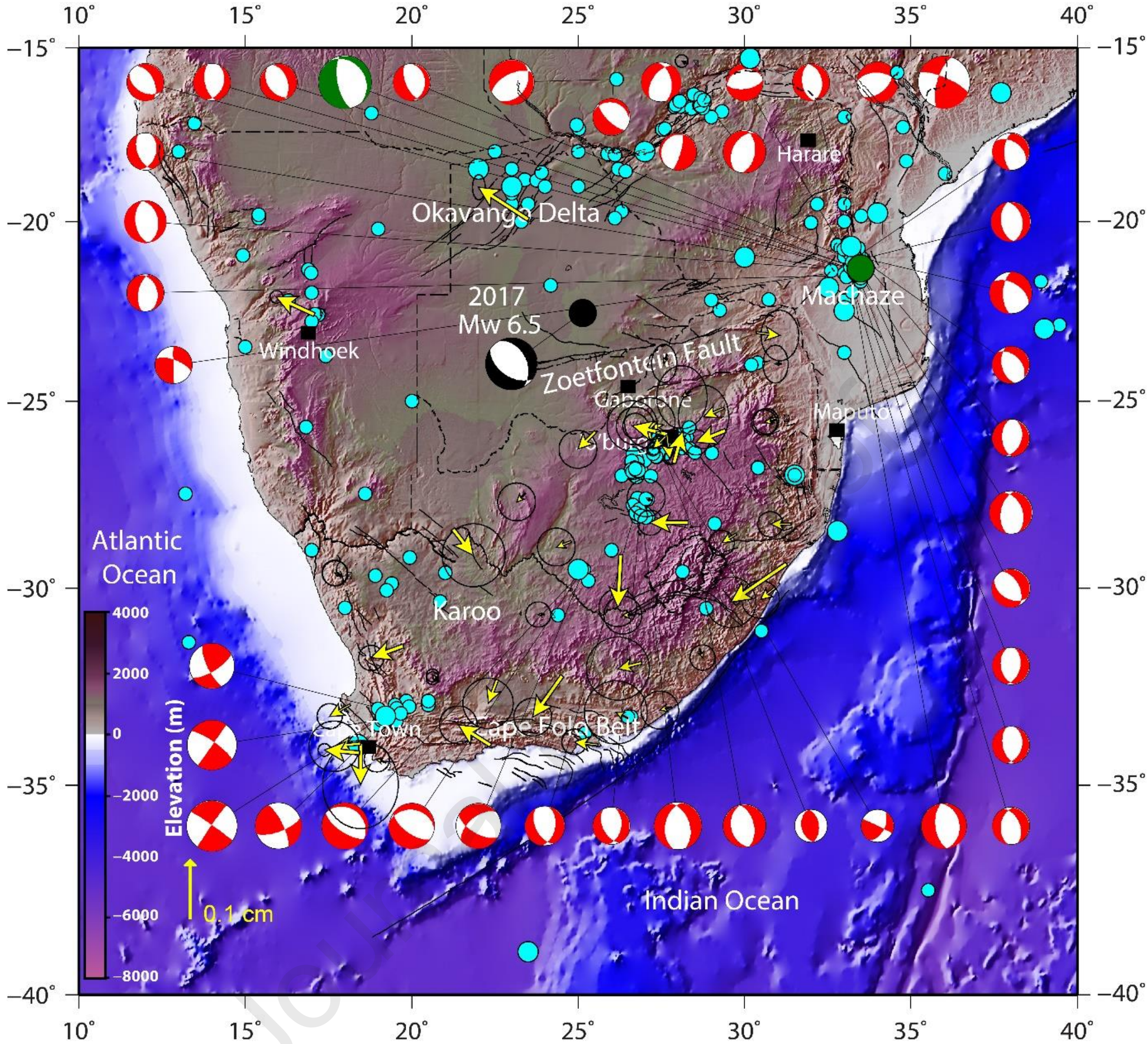

Figure 1: Seismotectonic background of southern Africa (light blue circles and red and white CMT focal mechanism solutions (SM1)), as updated from Meghraoui et al., (2016). Black circle is the location of the 3 April 2017 earthquake and its focal mechanism solution (black and white, CMT-Harvard, https://www.globalcmt.org/CMTsearch.html). The green and white focal mechanism is of the 23 February 2006 Machaze earthquake (Mw 7.0, Mozambique, green circle). GPS velocities (Nubia fixed, yellow arrow with 1σ error ellipse) are from Saria et al. (2014).

Table 1: Source parameters of the 3 April 2017 earthquake from various seismological centres.

Seismological Centre	Long. (°)	Lat. (°)	M_0 (Nm)	M_w	Depth (km)	Strike	Dip	Rake
USGS (Wpha)	25.15	-22.678	6.19×10^{18}	6.5	23.5	343	44	-62
GFZ	25.22	-22.66	6.3×10^{18}	6.5	27	331	37	-73
Geoscope	25.15	-22.678	5.86×10^{18}	6.4	29	333	36	-72
CMT Harvard	25.21	-22.54	7.01×10^{18}	6.5	30	332	41	-70
CGS (Pretoria) Midzi et al. (2018)	25.134	-22.565	-	6.5	26.5 ±2.5	340	46	-61
This study (InSAR)	25.134	-22.565	3.68×10^{18}	6.4	22 ±1.5	315	45	-80

In this paper, our objective is to better understand the earthquake generation processes in the 2017 Moiyabana earthquake area using near-field seismology and active tectonics coupled with remote sensing (geomorphic features and InSAR). Following the presentation of the seismotectonic context and a summary of previous works on the 2017 Moiyabana earthquake, we analyse the mainshock and aftershock sequence using the ~3-month records of portable stations supplemented by the seismograms of the permanent Botswana and South Africa seismic networks. The fault rupture geometry and focal mechanism solutions of the 2017 seismic sequence are determined along with the stress tensor distribution. Our InSAR study (from Sentinel-1 images) of the earthquake area provides the coseismic surface deformation, which coincides with the aftershock distribution and supports the inverse modelling of the fault-rupture parameters. The fault rupture geometry obtained from the seismic sequence and surface deformation is correlated with the composite fault escarpment identified SE of the earthquake area. We finally discuss the driving mechanisms and implications of the intraplate seismic activity and crustal deformation in southern Africa.

2 Seismotectonic setting and previous works

The collision of the Archean Kaapvaal and Zimbabwe Cratons between 2.7 and 2.6 Ga led to the formation of the Limpopo Mobile Belt, which constitute the site of the 2017 Moiyabana earthquake (Roering *et al.*, 1992; Brown *et al.*, 2008; Begg *et al.*, 2009). NW-SE trending shear zones within the Limpopo Mobile Belt are well identified by Bouguer anomalies (Ranganai *et al.*, 2002). The E-W trending Zoetfontein fault zone south of the earthquake location (Fig. 1.) developed in the lower Proterozoic era (Lekula *et al.*, 2018). Fourie *et al.* (2014) modelled the 380 m throw on the eastern part of the Zoetfontein zone and Lekula *et al.* (2018) attributed the western part to a 200 m graben structure. The crustal structure beneath cratons obtained from receiver functions and broadband seismic stations characterize the Moho average depth at 38 km, which is considered as the thinnest crust in the region (Nguuri *et al.*, 2001) and may explain the ~30 km thickness of the seismogenic layer (Midzi *et al.*, 2018).

The occurrence of the 2017 Moiyabana, Botswana earthquake prompted several works on its origin, driving mechanism, stress distribution and seismic strain accumulation. Kolawole *et al.* (2017) used high-resolution aeromagnetic, gravity data and InSAR analysis, and inverse modelling to investigate the Precambrian basement lithospheric structures and concluded that the fault rupture follows a distinct NW striking and NE dipping magnetic lineament within the Precambrian basement. Albano *et al.* (2017) show a model of the coseismic fault from InSAR results and infer a 20- km-long rupture plane, dipping 65° to the northeast, with a right-lateral component, and 2.7 m maximum slip at depth.

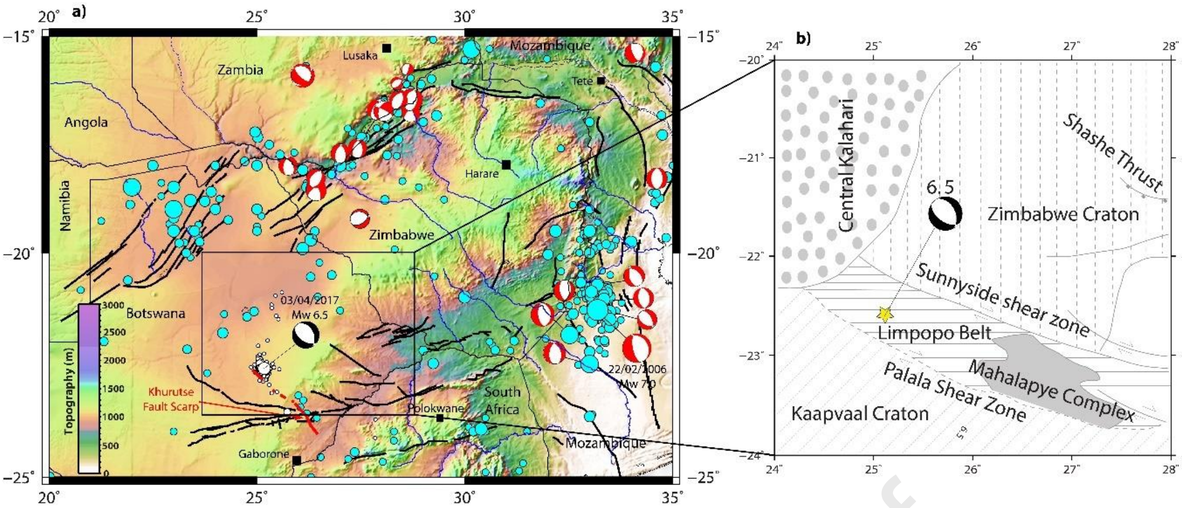

Figure 2. ***a)*** *Seismotectonic framework excerpt of the Seismotectonic Map of Africa (modified from Meghraoui et al., 2016) with focal mechanism (CMT-Harvard) of the 2017 Moiyabana mainshock. The red line is the inferred Khurutse fault scarp, cyan circles are background seismicity with magnitude $4.5 \leq M \leq 7.5$;* ***b)*** *Structural geology background of the 2017 earthquake area (modified from Brown et al., 2008). The mainshock is indicated by a yellow star.*

Gardonio *et al.* (2018) provide a seismicity study coupled with InSAR results to infer 6 cm of subsidence, 10 km along the dip and 30 km along the strike of the fault and suggest that the pore fluids pressure from a deep source at 29 ± 4 km might be the cause of the 2017 event. Moorkamp *et al.* (2019) investigated the epicentral area with seismic velocity and resistivity profiles and showed the collocation of a weak upper mantle and weak crustal structure between strong Precambrian blocks. They also show that although the modelled resistivity may indicate fluid activation on conductive structures, there is no evidence of the fluid migrating upward or a tectonic structure presenting to be the source of the 2017 Moiyabana earthquake within the vicinity. Fadel *et al.* (2020) suggest a link with the EARS by modelling the 3D crustal and upper mantle shear wave velocity structure of Botswana and concluded that the rift can be the source of a fluid driven from ~150 km depth of the north-eastern tip of Botswana to migrate to the edge of the Kaapvaal Craton and the earthquake area. Chisenga et al. (2020) modelled the Bouguer gravity and produced a high-resolution crustal thickness map of Botswana which suggests a correlation of the earthquake activity with the thermal fluid and elevated heat flow from EARS. Thomas (2020) also used the analysis of Sentinel images and provided an interferogram that suggests 9 to 10 cm total coseismic slip at the surface. Finally, Olebetse *et al.* (2020) studied foreshock and aftershock events recorded by the Botswana seismic network and suggest a correlation with local geological structures of the Kaapvaal Craton and Limpopo mobile belt. Although no field investigations were conducted after the mainshock, most studies correlate the 2017 seismic sequence with the tectonic reactivation in the Limpopo Mobile Belt due to thermal fluids and elevated heat flow linked to the EARS.

3 Mainshock and Aftershock Analysis

The mainshock of 3 April 2017 with M_W 6.5 was reported by several international seismological centres (Table 1) but the South African National Seismograph Network (SANSN) provided the most accurate location, as their seismic stations are in close proximity to the source. The epicentre location of the SANSN (Council for Geoscience, Pretoria) also includes data from the Botswana seismic network (Fig. 3). The largest aftershock with magnitude M_W 4.6 occurred west of the mainshock on 5 April 2017 at a much shallower depth (~10 km) than the mainshock.

Following the mainshock, an aftershock sequence was recorded from 8 April to 29 June 2017 by a temporary network and shows more than 900 earthquake records. Aftershocks that occurred prior to 8 April 2017 (i.e., date of installation of the temporary network as presented in Figure 3) and recorded by the Council for Geoscience (CGS) together with the Botswana Geological Institute (BGI) are excluded in our initial seismic sequence analysis (Figs. 5 a and b) due to fixed depth values (see figure in SM2). This early aftershocks-sequence consists of

65 events reaching M_L4.1 with a fixed constant 5-km-depth. The fixing of earthquake depths by the CGS is done in their routine seismic data analysis, as the sparse nature of the network makes it difficult to confidently determine depth values. The record of the seismic sequence (that benefited from the collaboration between seismic networks of the CGS and the BGI) includes seismic events with magnitude as low as M_L 0.8 with a decrease of daily occurrence rate from 101 to 20 seismic events within the first month of record (Midzi *et al.*, 2018). Following the mainshock, the seismicity decay obtained from the daily number of aftershocks conforms to the Omori's law (Fig. 4; Utsu et al., 1995).

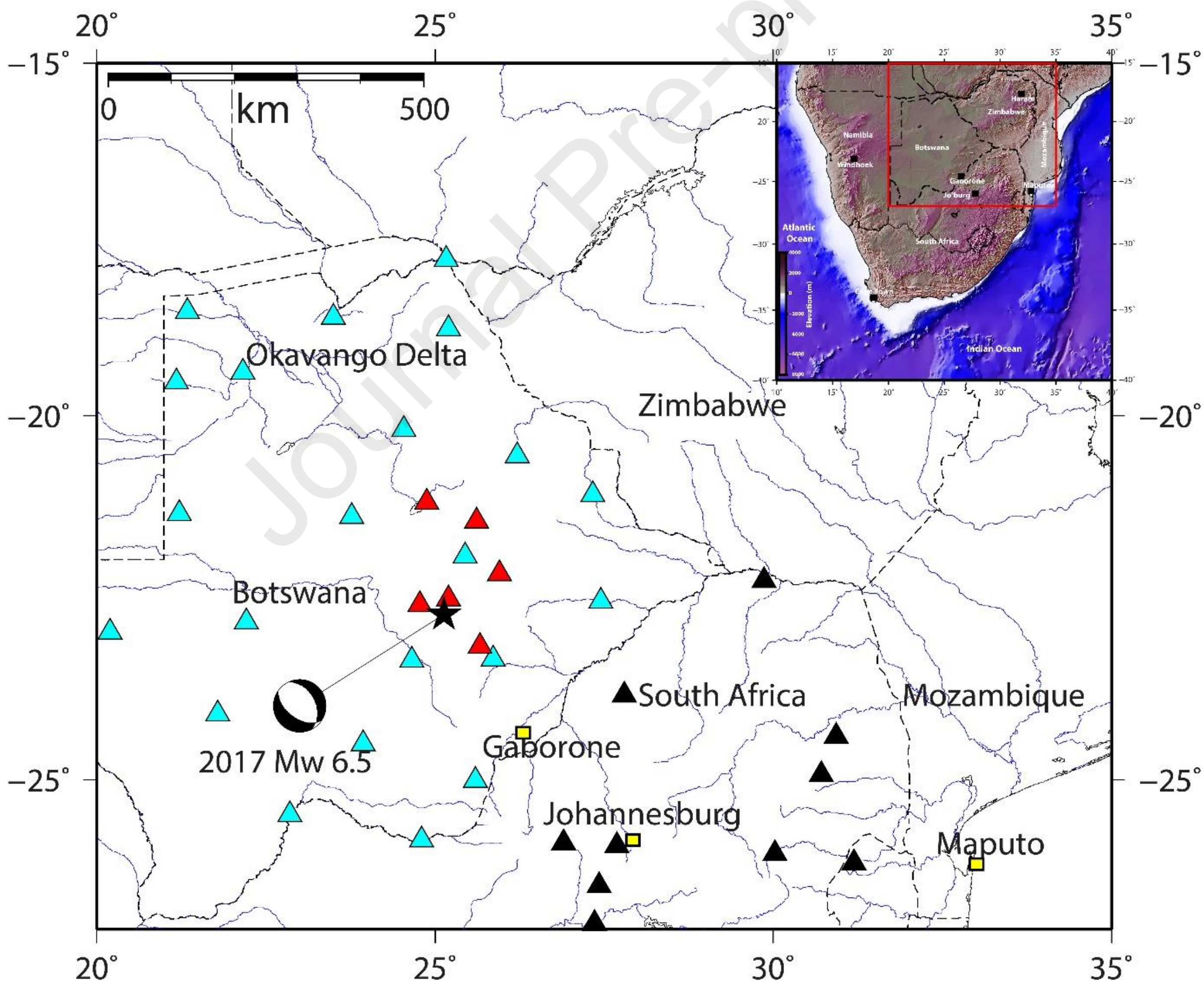

Figure 3. Seismic stations which recorded the mainshock (black star) and aftershocks. Focal mechanism is from Harvard CMT. *The seismic stations in cyan triangles are managed by*

Botswana Geoscience Institute and black triangles by Council for Geoscience. Portable seismic stations (red triangles) were temporarily installed and recorded aftershocks from the 8th of April to the 29th of June 2017. The inset image shows the location of Figure 3 in red square.

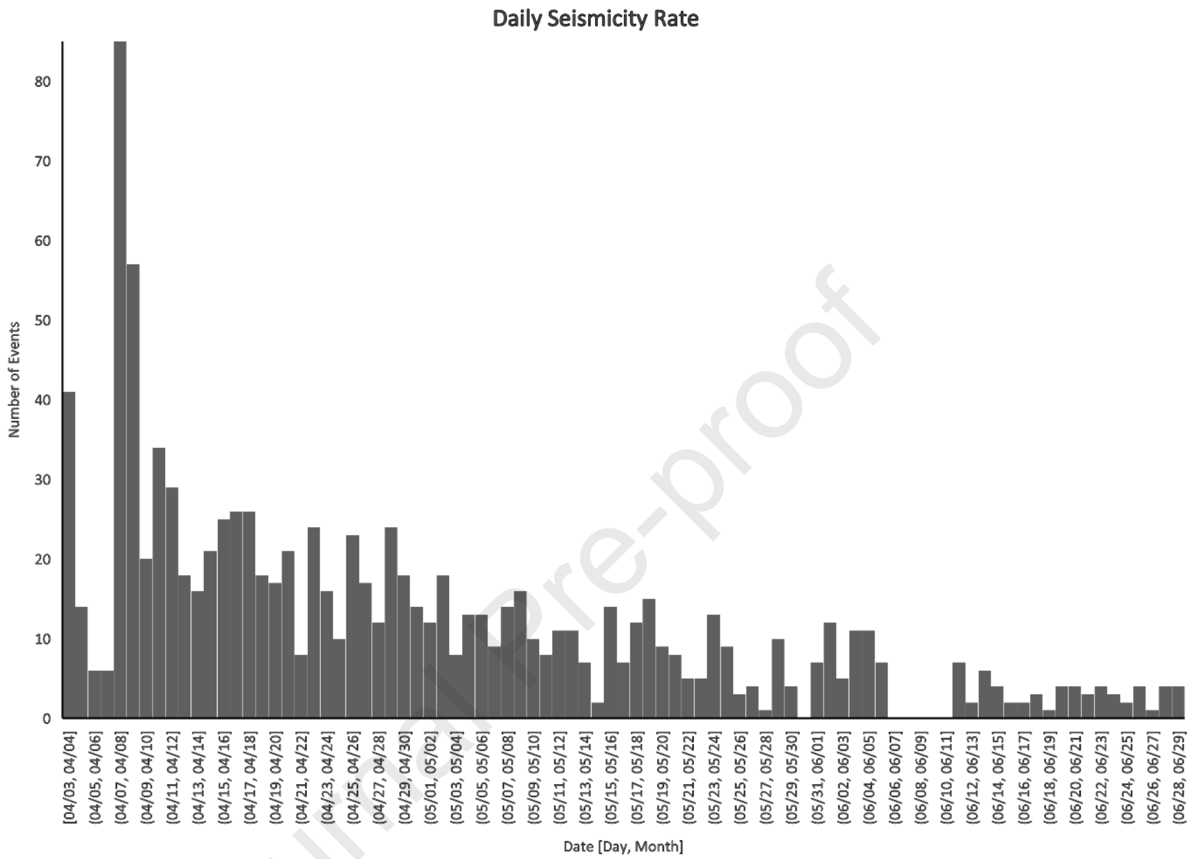

Figure 4. Daily number of seismicity recorded from the 3rd of April to the 29th of June 2017.

The initial earthquake locations were obtained using the modified HYPOCENTER program (Lienert *et al.*, 1986; Lienert and Havskov, 1995) in the SEISAN software package (Ottemöller *et al.*, 2018). This method utilises the interactive, least squares method to determine the location of the earthquake. The three-layer velocity model developed for South Africa (Midzi et al., 2010) was used in the location process (Table 2) resulting, on average, with epicentral and depth uncertainty of 1.5 km and 2.5 km, respectively.

Table 2: Velocity model used in aftershock locations (Midzi et al., 2010).

Modified depth to top of layer (km)	P-wave velocity (km/s)
0.00	5.80
20.00	6.50
38.00	8.04

The initial location of seismic sequence shows two clusters with a NNW-SSE trending western dense aftershock distribution and a N-S trending but sparse eastern aftershock sequence (Fig. 5a). The western aftershocks cluster includes the mainshock and largest aftershock whilst the eastern aftershock sequence, which is located about 20 km further east, includes one of the largest aftershocks with a magnitude M_L 4.2. The depth cross-section of the aftershocks shows the two clusters with a depth distribution of seismic events between 7 and 30 km for the western sequence, and between 4 and 12 km for the eastern aftershocks (Fig. 5b). The aftershocks also show a significant temporal eastern migration with the occurrence of the eastern seismic sequence mostly in June 2017 (Fig 6a). Fig. 6b illustrates the frequency of aftershocks versus the magnitude within the three months when temporary stations were deployed. The activity rate and b-value are 3.8 and 0.78, respectively, and we note the gap of earthquake magnitude between 4.6 and 6.5, implying that the M_W 6.5 event is a characteristic earthquake.

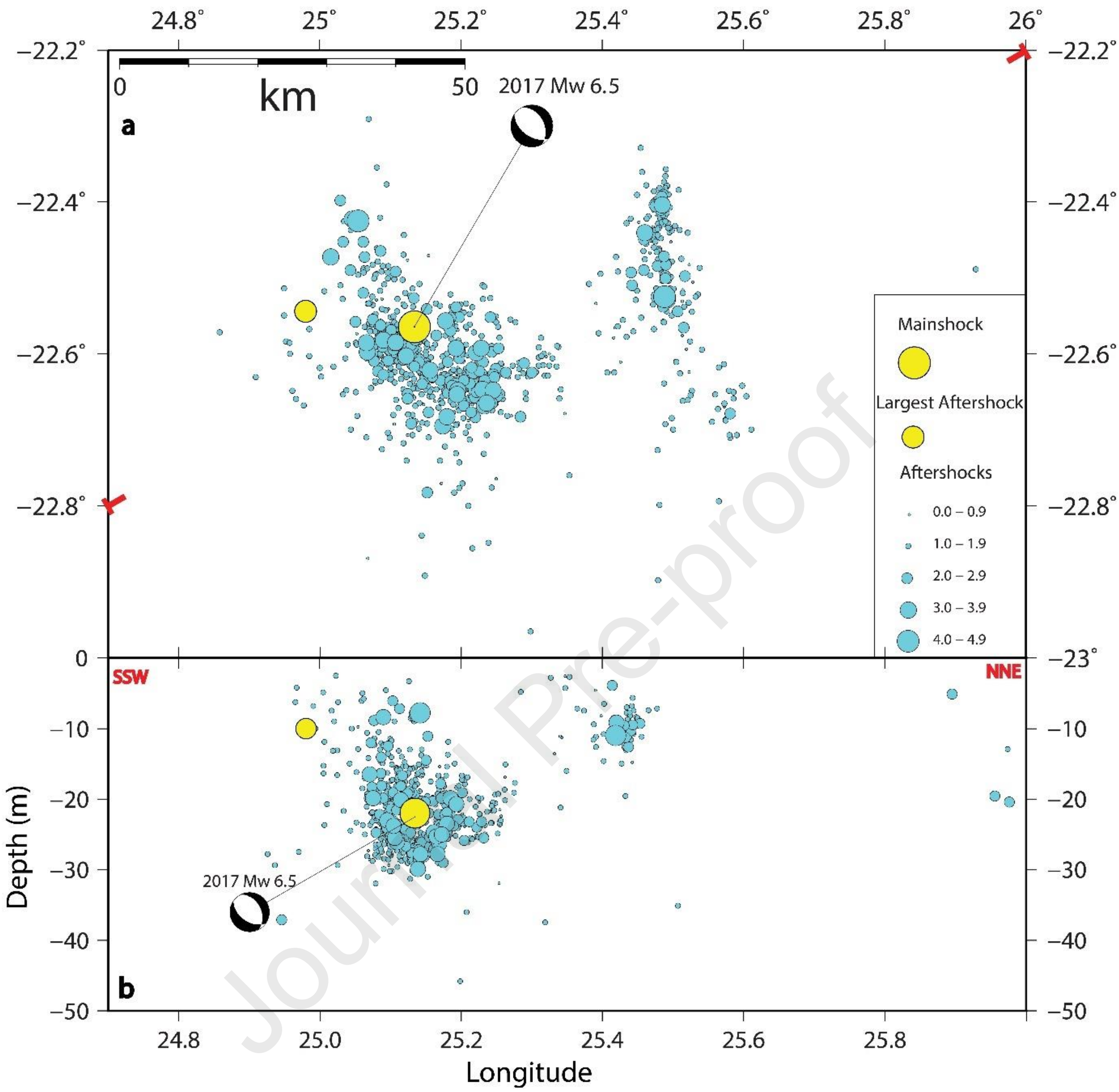

Figure 5. ***a)*** *Mainshock and the initial aftershocks sequence location of the 2017 Moiyabana earthquake with CMT-Harvard focal mechanism.* ***b)*** *Cross-section of the 2017 seismic sequence, as indicated by the T-symbols in Fig. 5(a), recorded by temporary network from 8 April to 29 June 2017 (cyan circles) following the mainshock.*

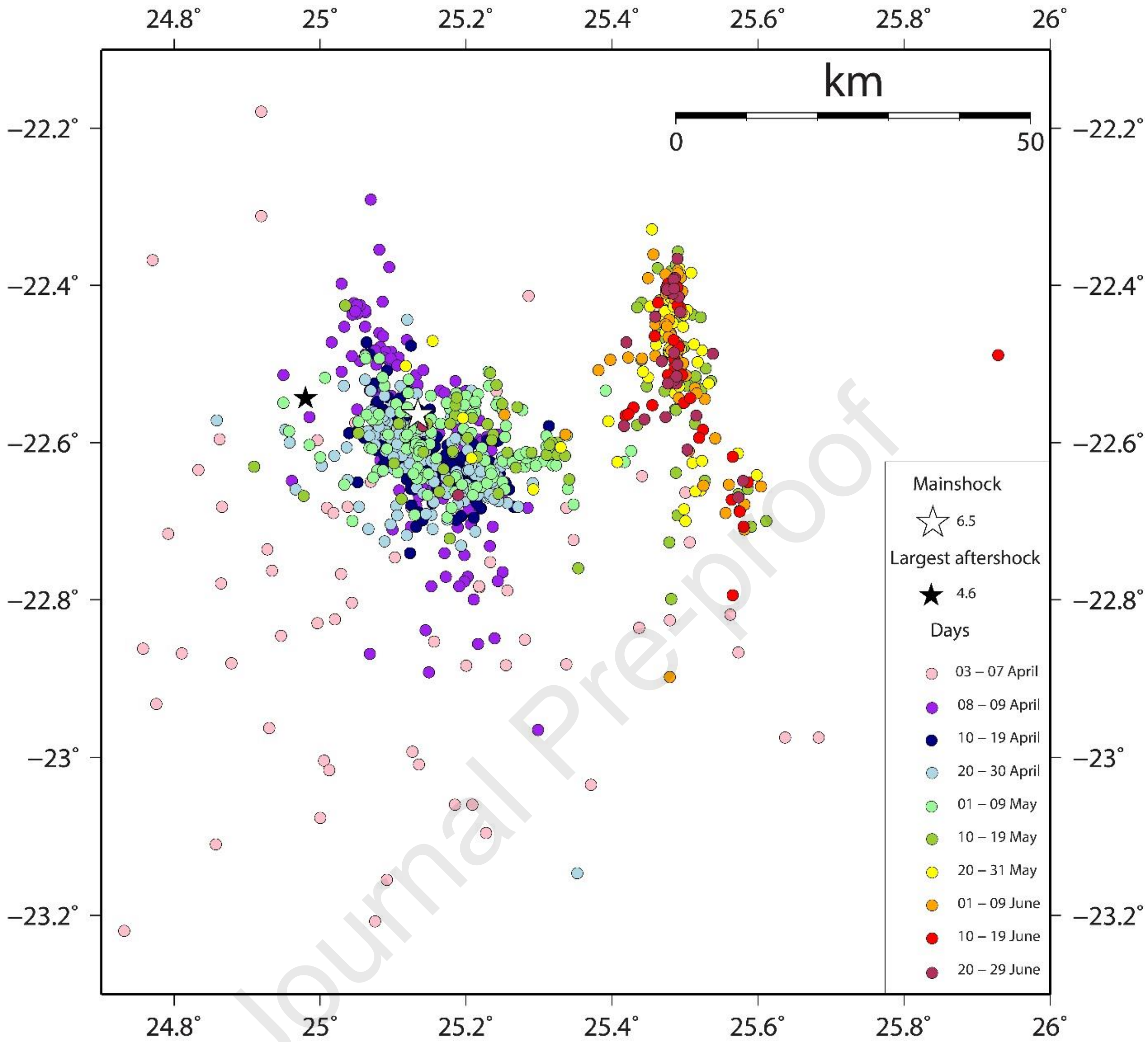

*Figure 6. **a)** Migration of more than 900 aftershocks (colour scale) recorded using the temporary network installed from 8 April to 29 June 2017 and 67 aftershocks (pink circles) recorded from 3 to 7 April 2017 by permanent stations. The eastern sequence occurred mostly in June 2017.*

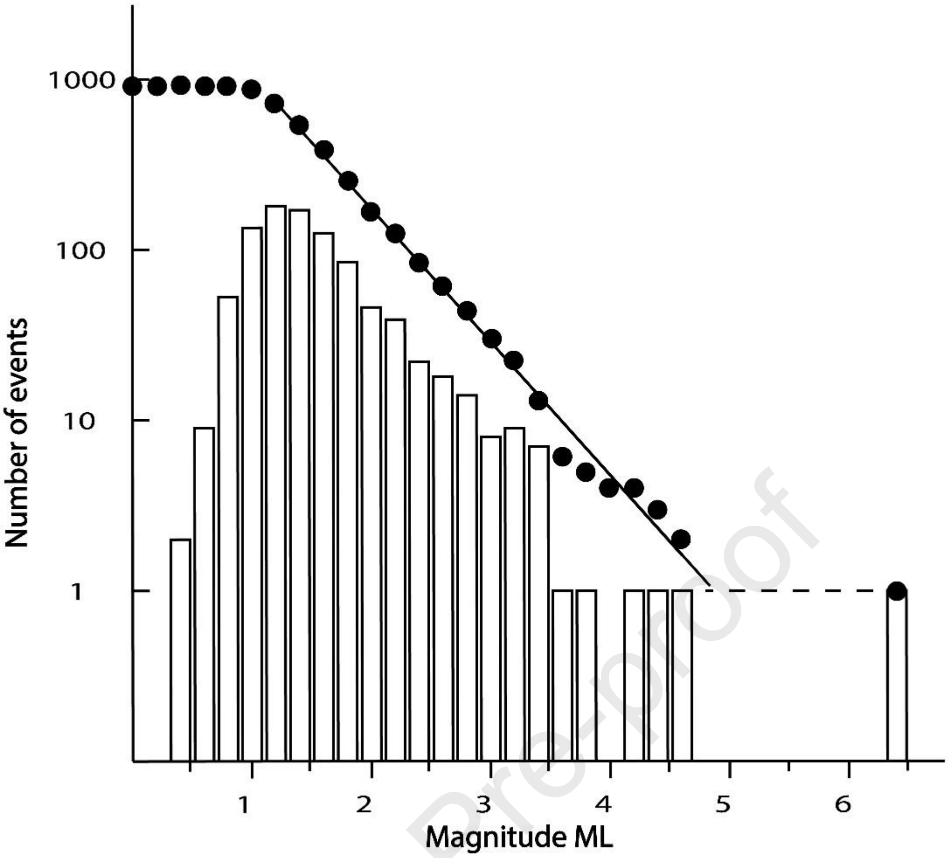

Figure 6. ***b)*** *Gutenberg-Richer relation Log N = 3.8-0.78M_L as applied to the 2017 earthquake sequence.*

In order to provide a complete description of aftershock distribution and improve their location and depth, the earthquakes were relocated using a double difference approach as implemented in the HypoDD program (Waldhauser and Ellsworth, 2000). In this seismicity analysis, we do not include aftershocks that occurred prior to the 8 April 2017 due to the distant location (> 150km) of seismic stations. The double difference approach uses cross-correlation between earthquake pairs to extract differential travel times from seismic stations. The cross correlation needs to occur from at least two seismic stations to further constraint the earthquake location. When a seismic station is not part of a pair, it does not contribute to further constrain the seismic source location. The computation reduces random noise in data by suppressing strong signatures of station geometry and allows a better location of the seismic source.

The HypoDD subprogram ***ph2dt*** is used to process first the seismic events into pairs, minimizing the RMS residuals between the observed and calculated travel time differences of P and S waves at same stations. 699 out of over 900 aftershocks were selected to be relocated considering the quality readings of P and S seismic waves, resulting in 1398 travel times. In this approach, we also consider the velocity model of Table 2, Vp/Vs ratio of 1.74. The aftershock analysis is made within the 50 km distance of the seismic sequence and at a maximum 170 km station distance, while previous studies of Midzi et al. (2010) provide the P-wave velocity 1-D model. The relocated earthquakes shown in Figs 7a and b are obtained from the double difference approach as implemented in the HypoDD program (Waldhauser and Ellsworth, 2000). The stability of the relocated solutions is satisfactory because six portable seismic stations are close to or within the aftershock sequence area and the P and S wave arrivals times allowed for an average 8500 iterations. Following the relocation process, the aftershocks distribution clearly shows the accurate concentration of seismic events in the seismogenic layer and upper crust (see figure in SM3). After relocation, most of the seismicity is located between 8 and 32 km depth, with most of arrival time RMS between 0.1 and 0.3 seconds (Fig. 7c). Taking into account the velocity model of Table 1, the depth uncertainties range between 0.7 and 2.1 km.

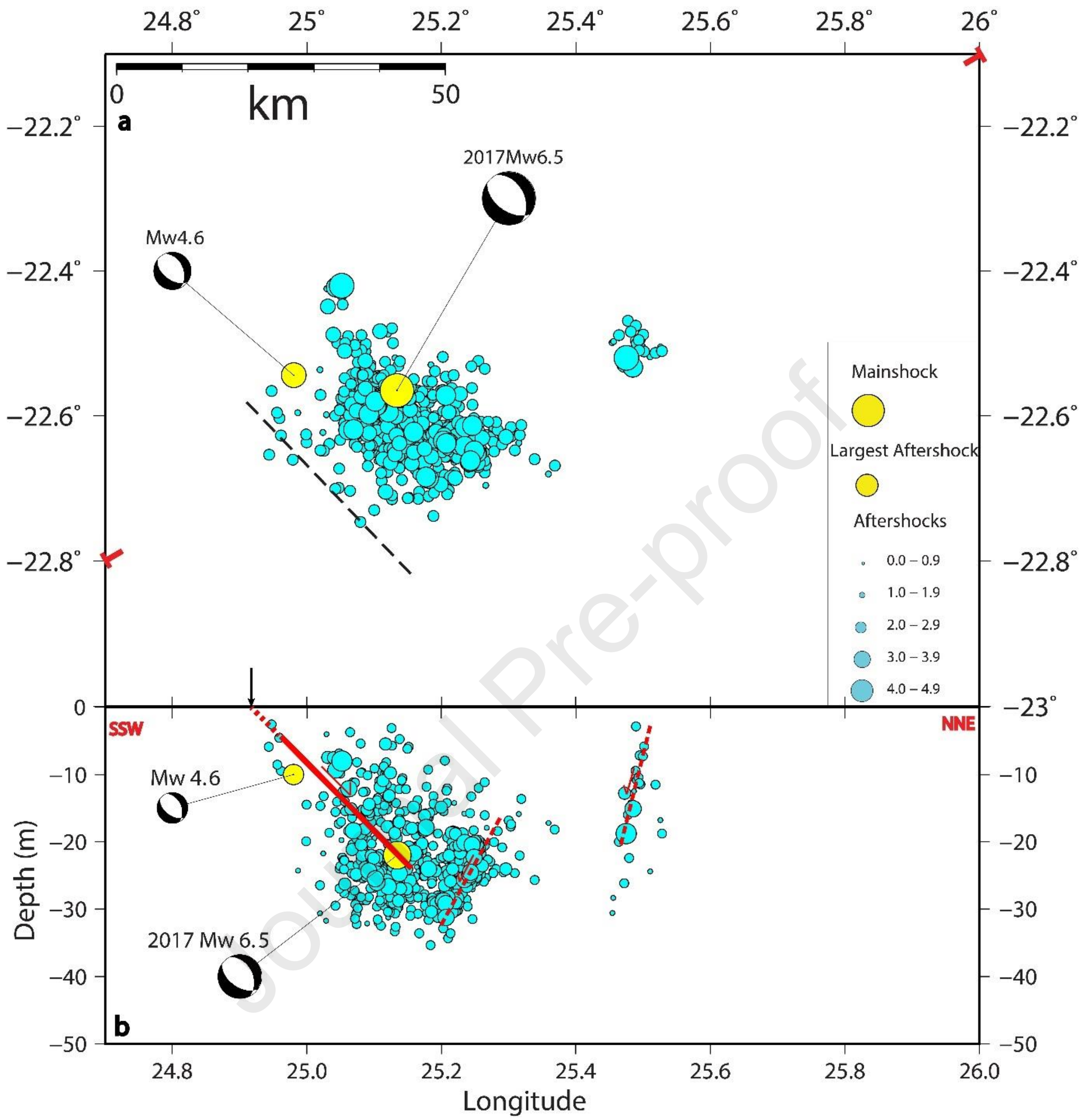

*Figure 7. **a)** Spatial distribution of aftershock locations obtained after relocation. Focal mechanism solutions of the mainshock and main aftershock are from CMT Harvard. The dashed line is the coseismic rupture tip inferred from the aftershocks at depth (Fig. 7b) and the analysis of InSAR fringes of coseismic surface deformation (see section on InSAR analysis). **b)** Aftershock sequence cross-section, as indicated by the T-symbols in Fig. 7(a), after relocation. Focal Red lines are the blind coseismic ruptures inferred from the*

mainshock and aftershocks sequence; the black arrow locates InSAR fringes of coseismic surface deformation (see section on InSAR analysis).

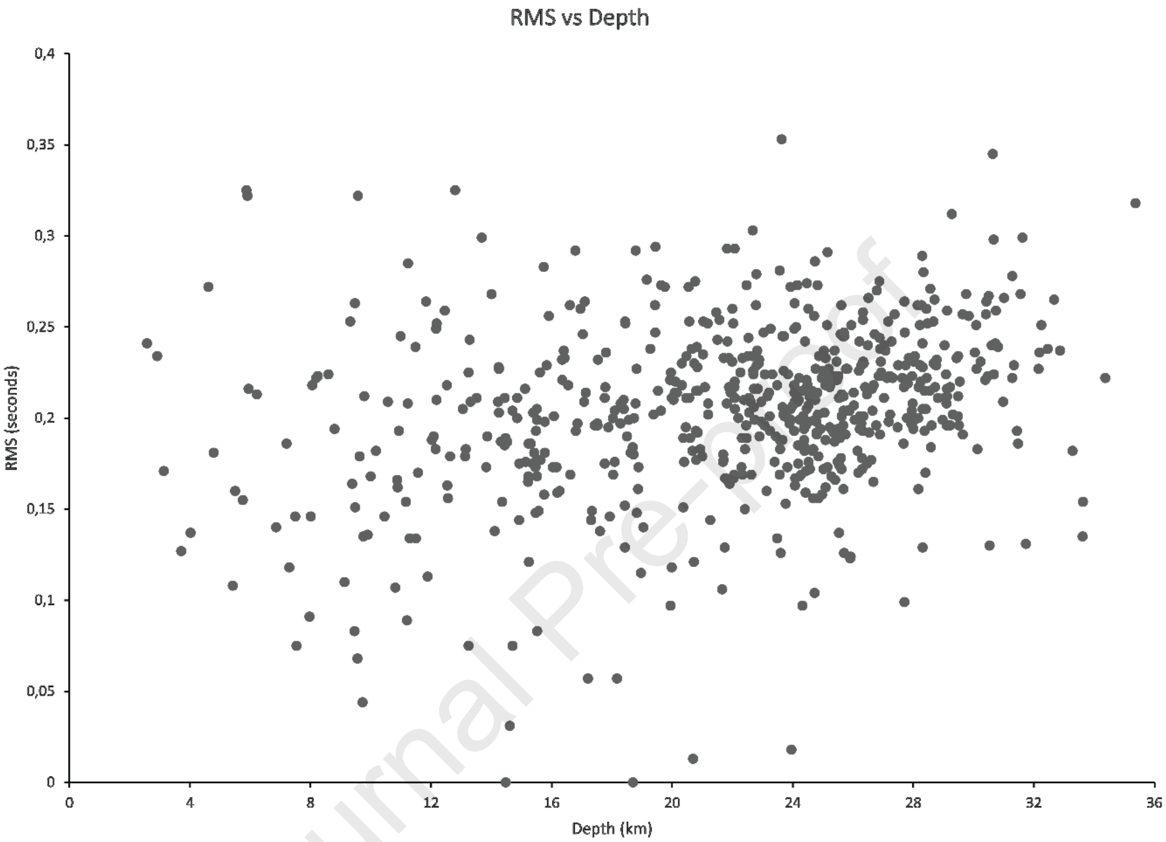

Figure 7. ***c)*** *RMS versus depth after relocating the aftershock sequence.*

Relocated events better show the clustering at depth (Fig. 7b). In the cross-section of Fig. 7(b), the western sequence of aftershocks shows sub-clusters between 10 and 30 km depth suggesting two conjugated fault ruptures. The eastern seismic cluster sequence appears at shallower depths (mostly between 5 and 15 km) and more clustered than in the SEISAN locations. They are well aligned marking a high angle west dipping rupture plane (Fig. 7b). The aftershock distribution and geometry of the inferred fault-ruptures at depth imply a graben-like tectonic structure within this part of the Limpopo Mobile Belt.

4 Focal Mechanism and Stress Inversion

The 2017 mainshock ruptured along a buried fault, which was not previously mapped. Therefore, any information on source geometry and stress orientation in the epicentral area is vital in understanding the driving mechanism. Focal mechanism solutions were calculated to indicate the maximum compressive horizontal and vertical stresses (Zoback and Zoback, 1989; Delvaux, 1993; Manzunzu *et al.*, 2017). The focal mechanism solutions for 46 selected aftershocks were computed based on first-motion polarities of P-wave (Ross *et al.*, 2018), using FOCMEC module in the SEISAN software package (Ottemöller et al., 2018). The degree of search varies from 2 to 20 degrees for different aftershocks. The focal mechanism solutions are shown in Fig. 8 and parameters are listed in SM4. The selected seismic events were those with signal to noise ratio above 2.0 and recorded by at least 5 stations with clear polarity readings.

311

312 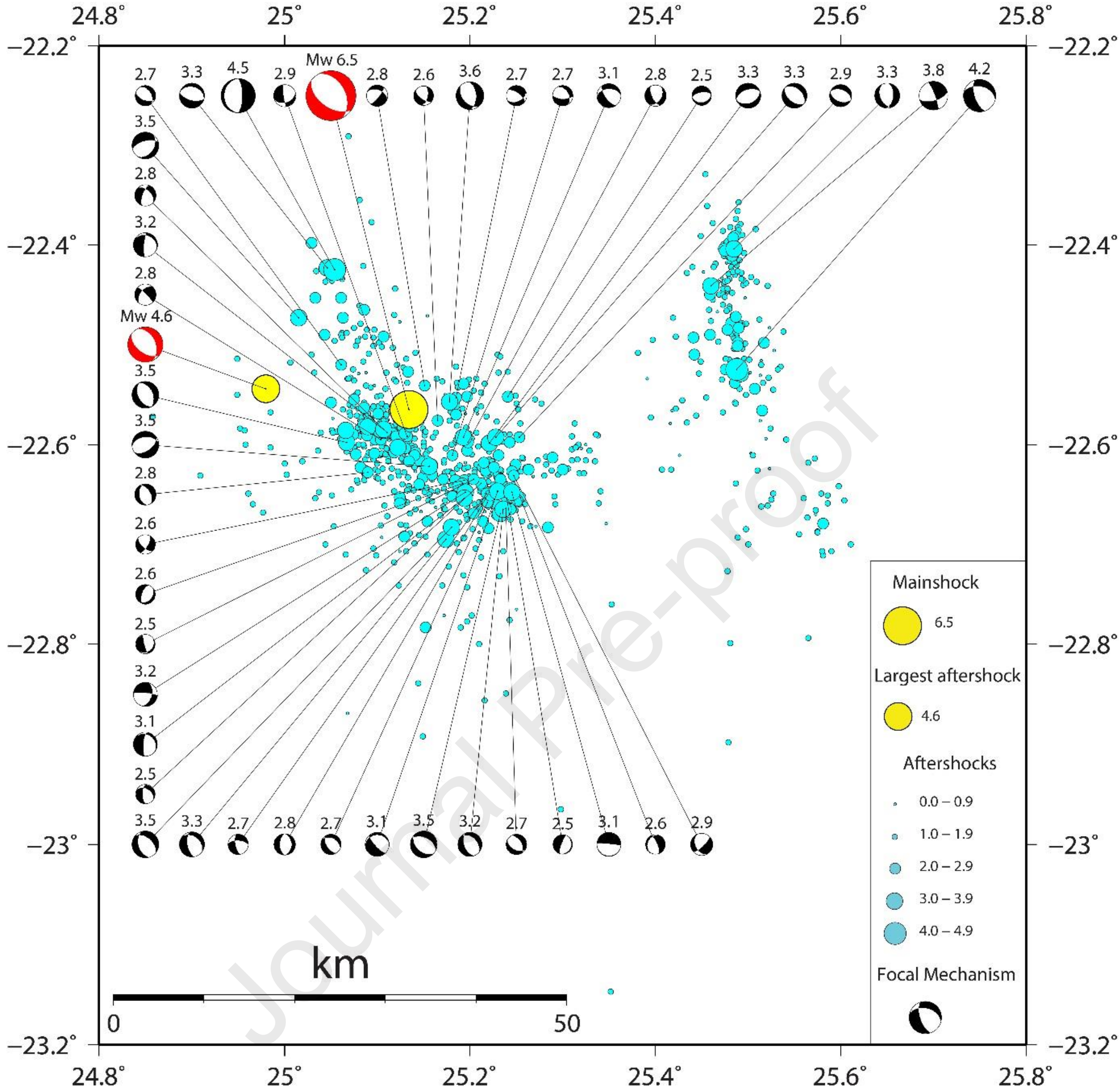

313 *Figure 8. Focal mechanism solutions of 46 selected seismic events (see also Table SM4).*

314 *Solutions are Schmidt lower hemisphere, the numbers above the solutions give the local*

315 *magnitude. Aftershock locations are as in Fig. 5(a). Mechanism of mainshock (in red) is from*

316 *Harvard CMT (https://www.globalcmt.org/CMTsearch.html).*

317

Focal mechanisms of aftershocks show normal faulting and few oblique mechanisms (Fig. 8 and Table in SM4). The mainshock and largest aftershock show normal faulting mechanism, with roughly NE and SE dipping nodal planes at 41° and 42°, respectively. The 2017 Moiyabana earthquake sequence occurred in an area with no known seismic history, therefore the stress regime is also poorly known. Focal mechanisms of mainshock and 45 aftershocks provide the opportunity to obtain information on the kinematic of faulting through stress inversion. For this purpose, two methodologies were used to conduct the stress inversion of the focal mechanisms compiled in this study: the improved right dihedron method (Angelier and Mechler, 1977) and the iterative rotational optimisation method as applied in the WinTensor program (Delvaux 1993; Delvaux and Sperner, 2003).

The dihedron method provides an initial approximate stress tensor that is then used as the starting solution for the rotational optimisation method (Delvaux and Barth 2010). Delvaux and Sperner (2003) implemented the rotational optimisation method as an iterative method that can be applied to minimise the misfit between data and model function for each earthquake. During optimisation, only the solutions which are compatible with the lowest misfit are utilised for stress inversion. Out of the 46 focal mechanisms (92 nodal planes) from the database, 30 (60 nodal planes), as well as 14 (28 nodal planes) are compatible with a NE-SW extension under normal faulting regime (Fig. 9). The later analysis with 14 focal mechanisms is performed to test the results after optimising the dataset further for more compatibility.

The locations on a normal fault system along NW-SE trending shear zones of the Limpopo Mobile Belt show the influence of the geological background. Most of aftershocks are characterized by average NW (340°) striking with NE dipping fault planes, consistent with the stress distribution and NE-SW extension. The predominant normal faulting mechanism indicates an extensional neotectonic regime in the epicentral area.

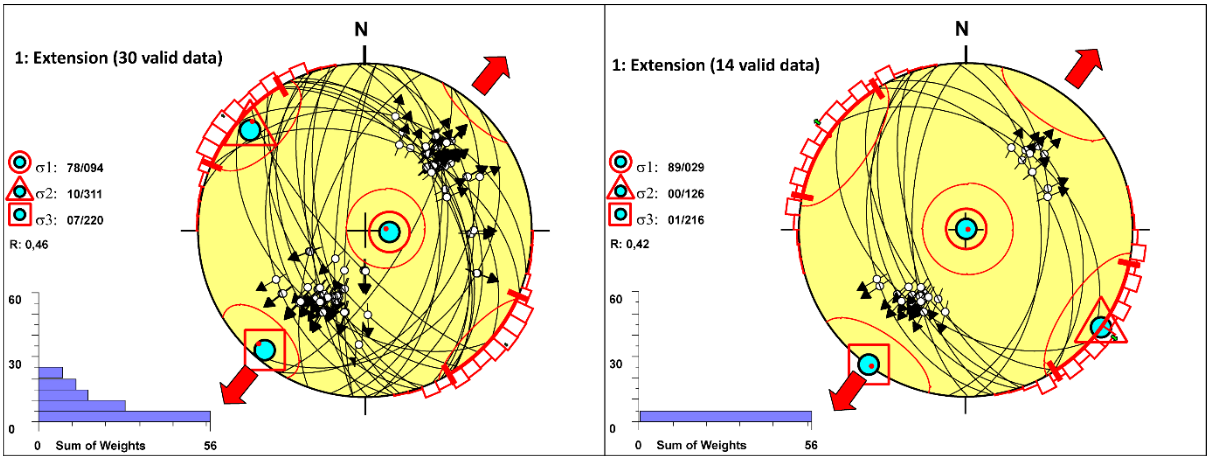

Figure 9. Stress inversion of 2017 earthquake aftershocks obtained from the WinTensor programme of Delvaux and Sperner (2003). Schmidt diagrams show nodal planes (black lines), with Left: Solution from 30 focal mechanisms taking into account all solutions, Right: Solution from 14 focal mechanisms with similar strike, dip of fault planes and slip vectors (black arrows). The stress tensor distribution (cyan circles) with σ1 in red circle, σ2 in triangle, σ3 in square, indicates 220°N and 216°N as the main extension directions (large red arrow). The ratio R (0.46 and 0.42) expresses the predominance of extensional stress state, and histograms sum of weights that verify the stress tensor.

As shown by the analysis of the 2017 Moiyabana earthquake data, its seismotectonic background and nearby geophysical studies such as magnetics and resistivity, the stress field confirms the large-scale extensional forces that may result from elevated heat flow, thermal fluid migration and SW extension of the EARS (Andreoli *et al.*, 1996; Delvaux and Barth, 2010; Meghraoui *et al.*, 2016; Materna *et al.*, 2019; Moorkamp *et al.*, 2019; Chisenga *et al.*, 2020). The active deformation across the Limpopo Mobile Belt and southern African intraplate domain shows N36E to N40E average extension direction with low level strain rate (~1 nanostrain/yr.; Malservisi *et al.*, 2013), and although the 2017 seismic source is relatively deep (> 20 km), the existence of thermal fluids and active tectonics with surface deformation suggests the presence of a seismic cycle and associated elastic strain release.

5 Surface deformation

5.1 InSAR Analysis

The SAR (Synthetic Aperture Radar) frames examined in this study are two pairs of ascending Sentinel-1A images that cover the earthquake area (Fig. 10). The used radar images before and after the 2017 mainshock were obtained from the archives of the European Space Agency, and interferograms are processed using GMTSAR (Sandwell *et al*., 2011).

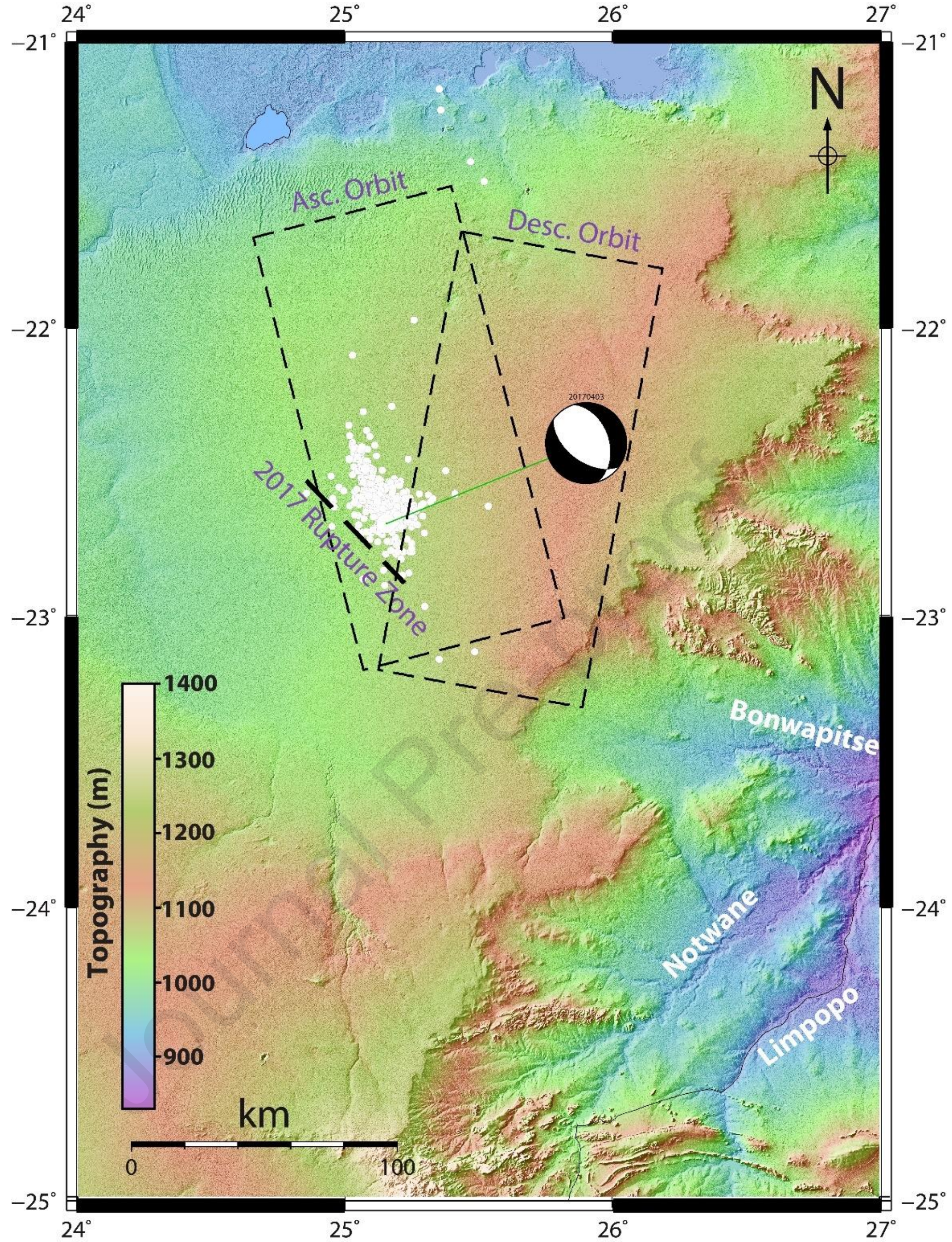

Figure 10. Frame of ascending and descending tracks of Sentinel-ESA-SAR images crossing the 2017 earthquake area. We observe that only the ascending track covers the whole 2017 earthquake area. Thick dashed line is the inferred 2017 Moiyabana earthquake rupture zone and small white circles show aftershock distribution. Focal mechanism of mainshock is from Harvard CMT. Background topography is from SRTM1'.

The SRTM Digital Elevation Model (30 m resolution) is used to remove the topographic phase component from the original interferogram (Farr et al., 2007). The spatial filter (Gaussian) is applied to obtain the interferogram (Fig. 11), before proceeding with the unwrapped interferogram using the Snaphu software (Chen and Zebker, 2002). Finally, the unwrapped phase was converted into Line-Of-Sight (LOS) displacement (Fig. 11). The obtained interferogram from a pair of ascending images (2017-03-30 and 2017-04-11; 1A/1A) shows clear lobes of LOS displacements (Fig. 11). The interferogram from ascending tracks show a consistent fringe distribution with ~40-km-long and ~20-km-wide NW-SE-trending lobes. The LOS measurements display ground displacement of the SW and NE blocks, respectively, indicating a clear straight limit between lobes that represents the fault zone on the SW edge of the lobe. For ascending tracks, the maximum and minimum values of the LOS displacement range from 4.2 cm to 5.6 cm for interferogram (Fig. 11) from which we estimate a total of 3.86 – 5.15 cm of vertical surface deformation across the fringes. The analysis of the Sentinel-1 interferogram shows a NW-SE elongated and 40-km-long surface deformation consistent with a blind fault rupture geometry. The interferogram also shows a surface deformation with subsidence coincident with the 2017 earthquake sequence location and normal faulting mechanism consistent with the source time function (http://geoscope.ipgp.fr/index.php/en/catalog/).

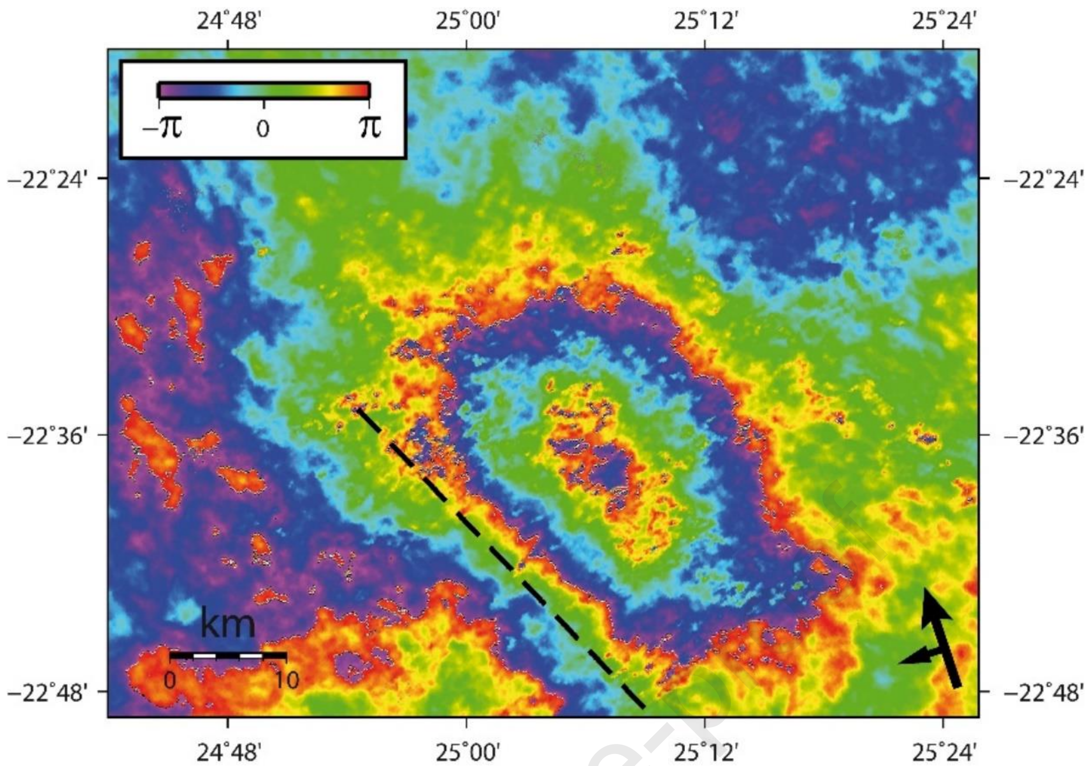

Figure 11. Fringes and lobes of interferogram of the 3rd of April 2017 Botswana earthquake. The dashed line is the projected fault rupture with respect to surface deformation with subsidence (~4.2 – 5.6 cm in LOS). The black arrow (small arrow) is the Sentinel satellite track with side look.

5.2 Earthquake Rupture Model

Rupture and slip models were developed using the ascending phase interferograms and the related coseismic deformation. To minimize the afterslip and/or postseismic effects, the modelling is based on interferograms obtained from the earliest coseismic pairs of Sentinel scenes (Figs 11, 12 a and b). In order to constrain the earthquake rupture geometry and slip distribution at depth, different solutions were tested using fault parameters for the inversion modelling that confirm the InSAR surface deformation.

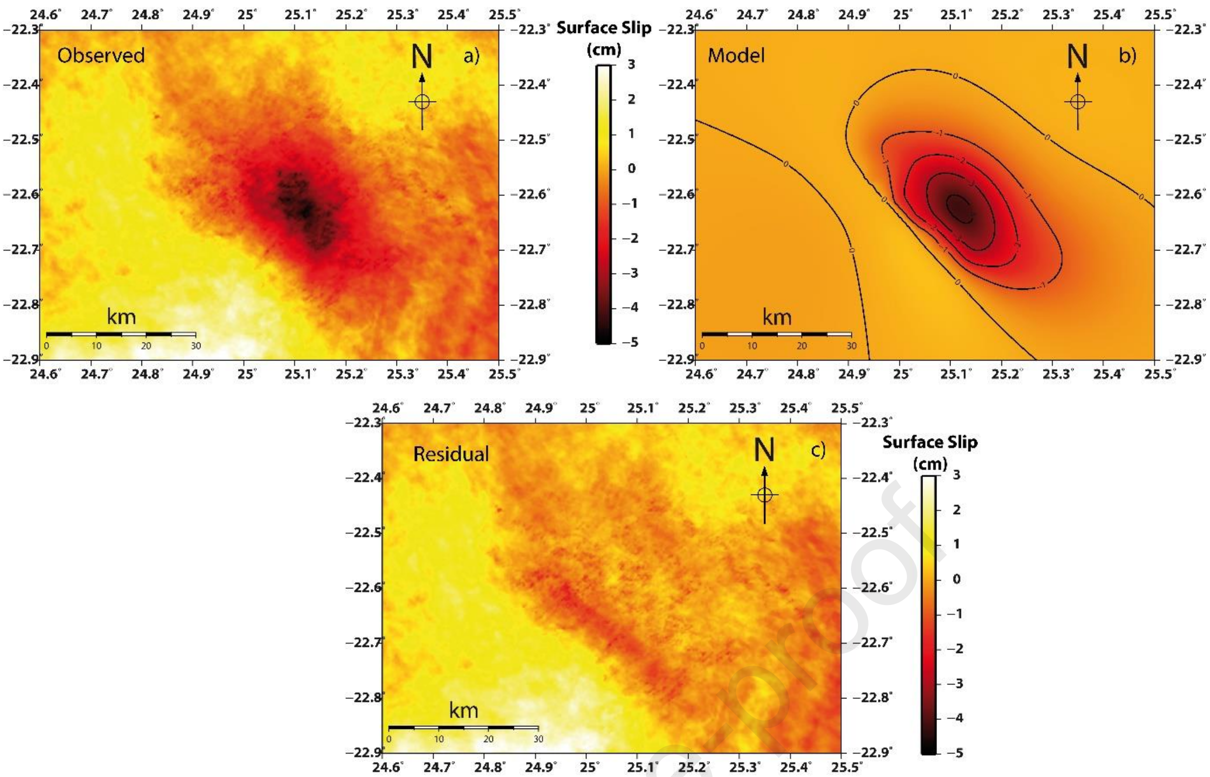

Figure 12 ***a)*** *Unwrapped SAR data interferogram with surface slip distribution.* ***b)*** *Modelling of surface deformation from the inversion of InSAR data.* ***c)*** *Residual of InSAR results versus model.*

The inversion modelling was performed for the dip slip and strike slip component of deformation using the Poly3D method considering triangulated surfaces as discontinuities in a linear, elastic, homogeneous, and isotropic half-space (Maerten *et al.*, 2005; see the details of the method in SM5). The blind coseismic fault coincides at the surface with the inflection area in between the uplift and subsidence lobes (see the fault tip trace in Figs 7b and 11). Considering different fault dimensions and dip angles, we performed a series of inversions that lead to the best fit (with 95% data variance) for the 3D surface slip obtained on the 315°, dipping 45°, -80° rake, ~40-km-long and ~22-km-wide fault geometry with a seismic moment of 3.68 x 10^{18} Nm (Table 1, Fig. 13).

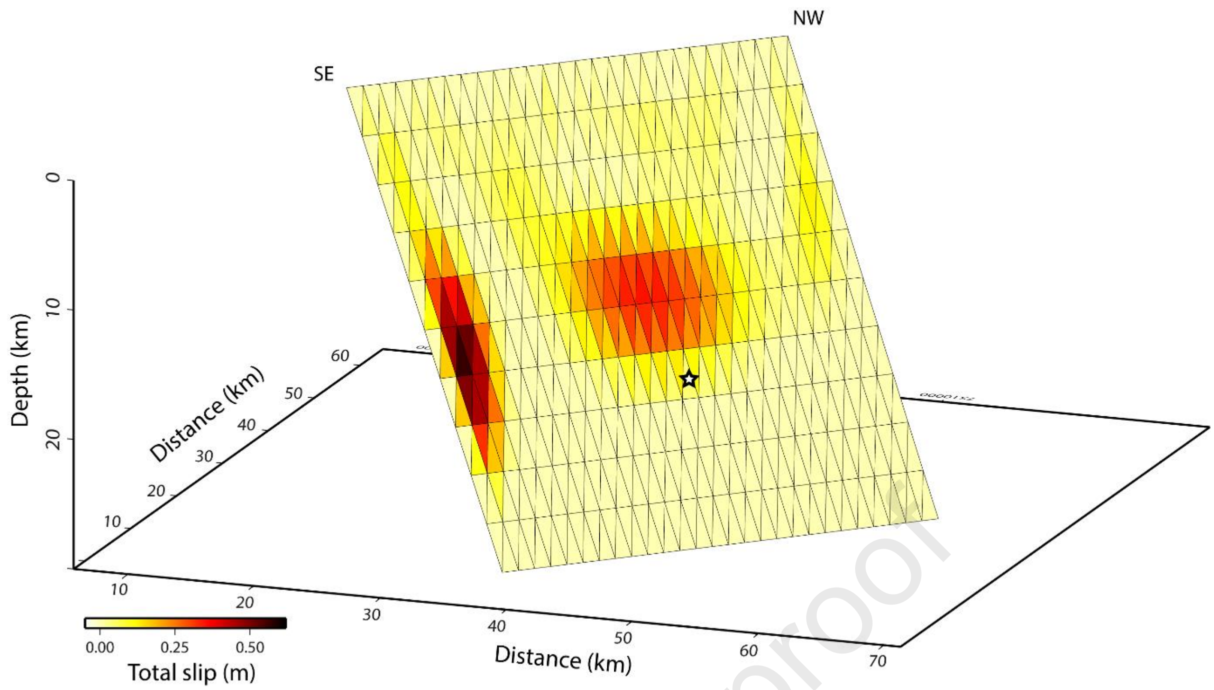

Figure 13. Model of fault rupture with slip distribution reaching 50 cm at depth, as inferred from the inversion of InSAR data and surface deformation. The star indicates the inferred 3rd April 2017 earthquake hypocentre.

The best fitting model shows a maximum slip of 50 cm at a depth of 22 ± 1.5 km and the existence of two asperities along the fault which agrees with the observed western seismic cluster (Figs 7a and b). Observed interferograms are compared to the inversion models in order to minimize the residual fringes with RMS misfit (Fig. 12c). The residual signals in Figure 12c (~1 cm) could be attributed to the atmospheric delay signal, the unwrapping error, and the surface motion caused by the post-seismic afterslip and aftershocks. As shown in Figure 14, the modelling allows to test the 0.744 cm RMS against the 0.4 smoothing and 0.23 roughness of the coseismic rupture. The location of the InSAR displacement and inferred blind fault rupture with NW-SE elongated lobes suggests a correlation with ~30-km-long buried fault that belongs to the Limpopo Mobile Tectonic Belt and can be correlated to the Khurutse fault scarp visible further southeast.

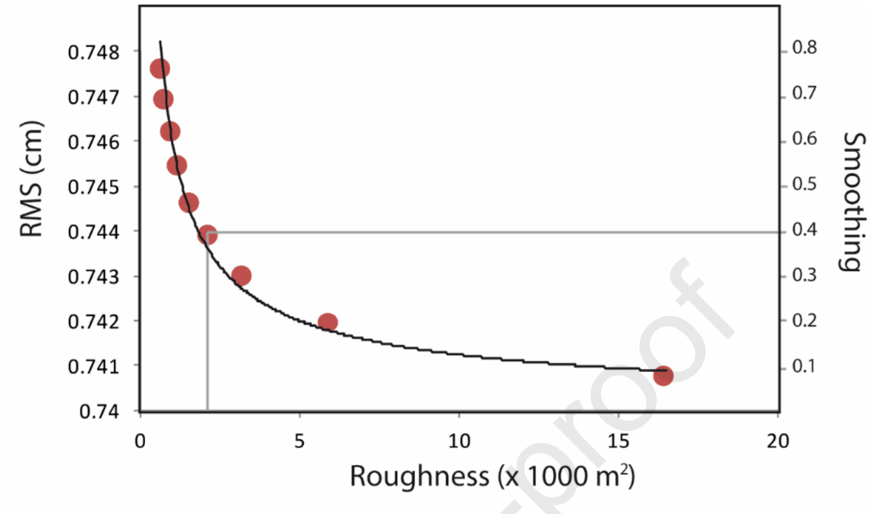

Figure 14. RMS misfit (minimize the residuals) obtained from the comparison between interferograms and inversion models of Figures 12a and b), residual of Figure 12c, and slip distribution of Figure 13. The 0.744 cm RMS and 0.4 smoothing (grey lines) correspond to the best compromise for the slip distribution on the fault plane.

6 Khurutse Fault Scarp and Long-term Seismic Cycle

The interplay between tectonic processes which build up topography and the surface processes which tear them down over time, in days to millions of years, are what defines tectonic geomorphology (Burbank and Anderson, 2001). Thus, the study of tectonic geomorphology can indicate geological linear structures from past fault activities. Such studies can be done using for instance GPS data, providing a rate of deformation on the Earth's surface such as the spatial deformation pattern caused by an earthquake. The displacement field of the earthquake can be measured from the deformed ground surface, subsequently delineating the relationship between seismic characteristics, displacement gradient and rock properties.

The Khurutse fault scarp is visible on topographic maps (both SRTM 90 m and 30 m resolution; Farr *et al.*, 2007) southeast of the 2017 M_W 6.5 earthquake (Figs 15, 16 and 17a). Four cross section profiles of the faults scarp (Fig. 17b) were plotted using the differential GPS data collected at sites indicated in (Fig. 17a).

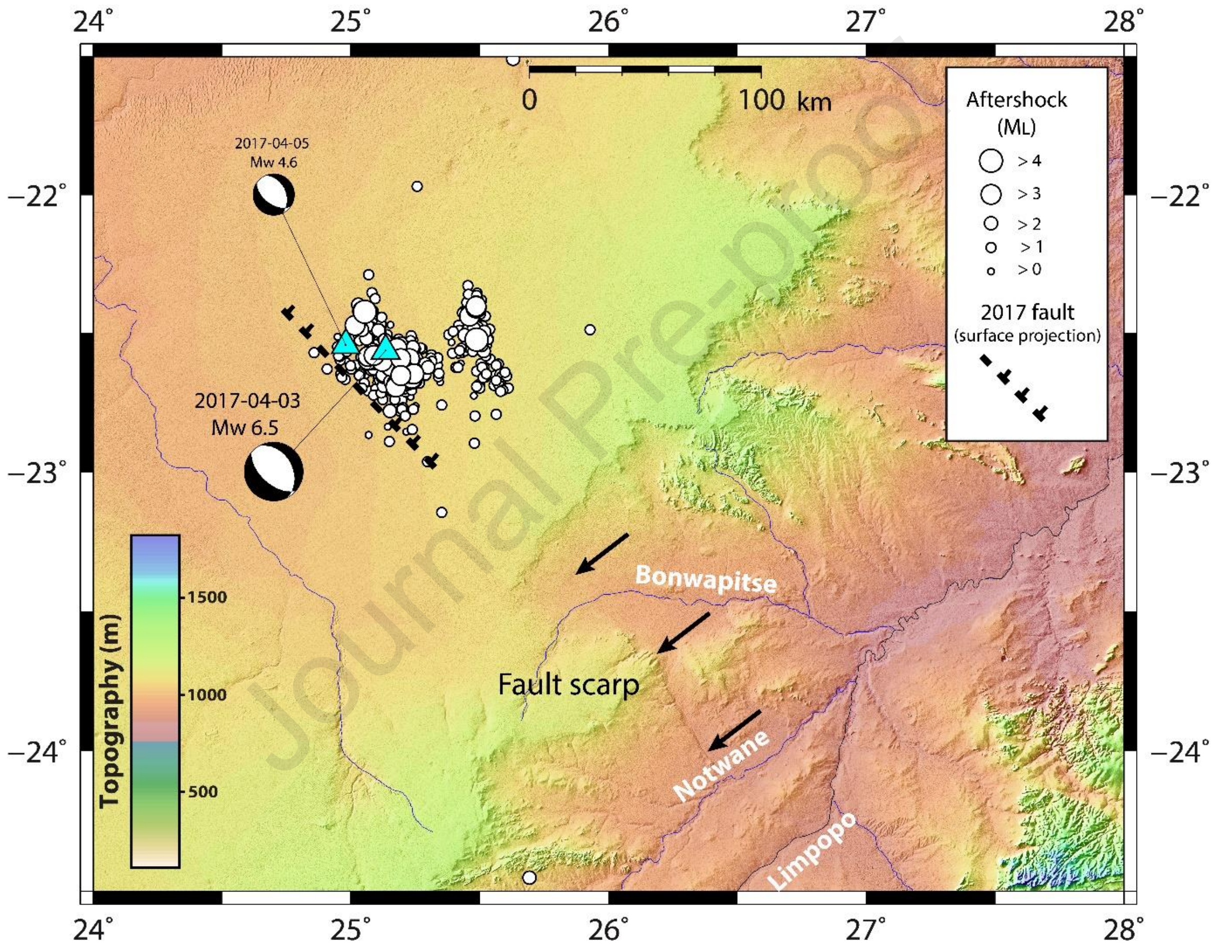

Figure 15: Identification of the Khurutse cumulative fault scarp (black arrows) southeast of the 2017 earthquake rupture indicated using a dashed line located from the projection of InSAR rupture (see Fig. 11). Also shown are the focal mechanisms of the mainshock and largest aftershock as presented in Tables 1 and SM4. Details of Khurutse fault scarp

morphology are in landscape photos of Fig. 16 and map of Fig 17a. Background topography is from Shuttle Radar Topography Mission (SRTM) 1" data.

Figure 16. Khurutse fault scarp with significant topographic offset. Left is fault scarp (view facing east) near profile A (24.004°S, 26.376°E) of Figs 17a and b; Right is fault scarp (view facing west) near profile B (23.967S, 26.350E) of Figs 17a and b. Fault scarps show composite and cumulative geomorphic structures that suggest repeated coseismic surface deformation.

The exposed NNW-SSE trending and ~80-km-long Khurutse fault scarp southeast of the 2017 epicentral area is aligned with the 2017 coseismic rupture and aftershock sequence (Fig 15). The escarpment is orthogonal to two main erosion valleys formed by different rivers and streams and crosses mainly Phanerozoic sediments. To the southeast, and although crossing an erosional valley, the fault scarp morphology is prominent and visible on left and right river channel banks (Fig. 17a) (Williamson, 1996). Differential GPS measurements of profiles across the fault scarp shows topographic offset ranging between 16.6 ± 1 m and 43.5 ± 1 m (Fig. 17b). All geomorphic profiles display a composite and sharp scarp morphology that reflects a cumulative surface deformation. The fault scarp height variation depends on the background geology and erosion effect and shows minimum and maximum topographic offsets in profiles A and D, respectively. That the linear morphology and scarp shape remain visible in the Limpopo Mobile Belt, is indicative of recent tectonic movement that may have resulted from incremental surface slip during past earthquakes.

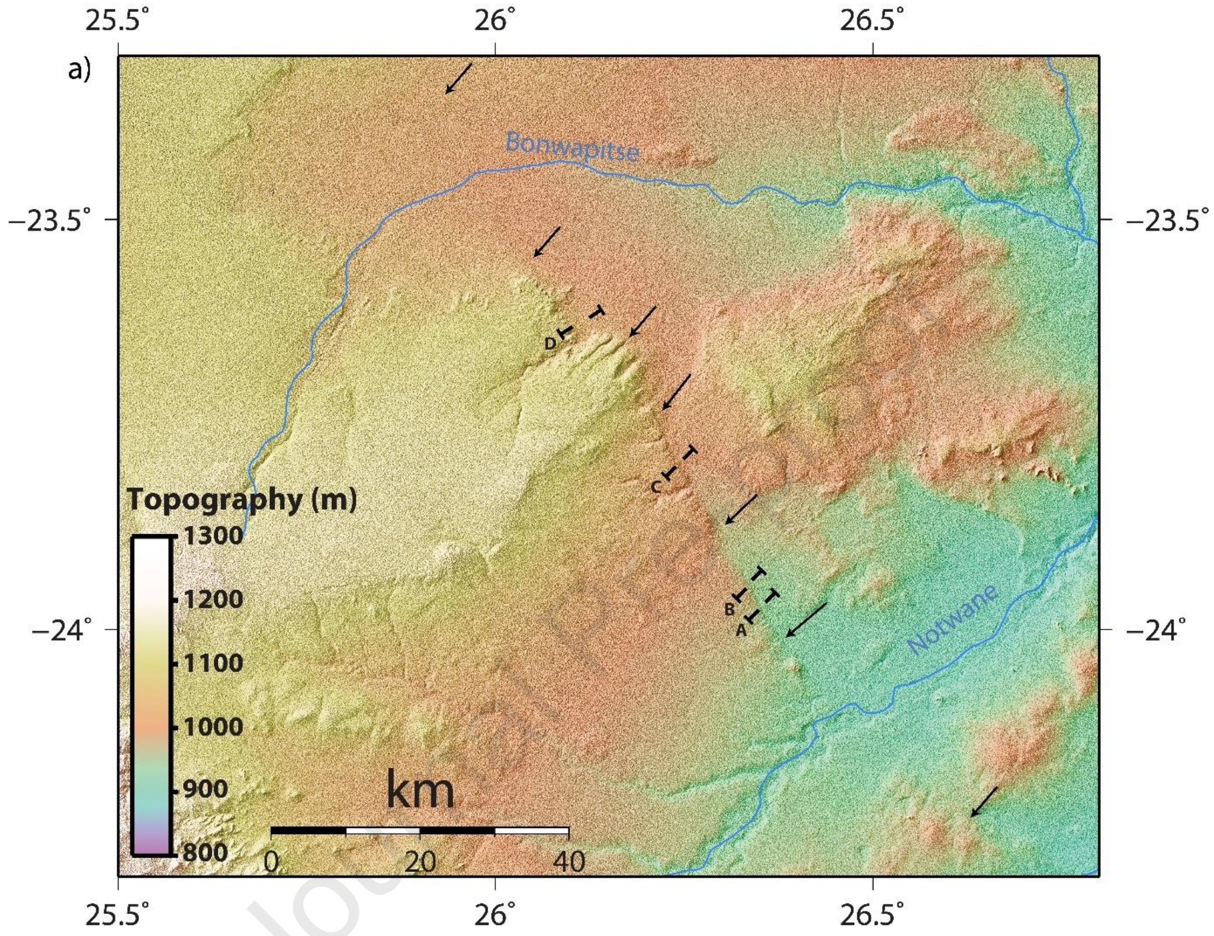

*Figure 17. **a)** Detail of the Khurutse fault scarps (arrows, see also arrows in Fig. 15) with location of the cross-section profiles of Fig. 17(b) denoted A to D (background topography from SRTM 1" data).*

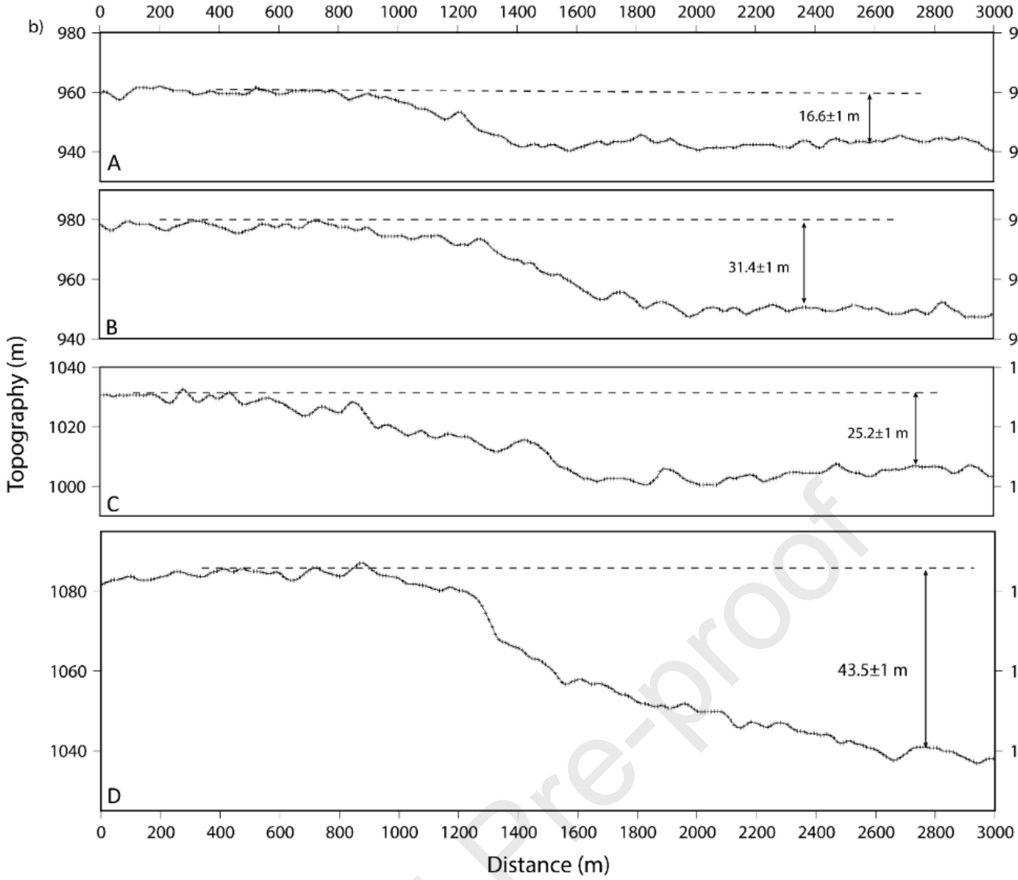

Figure 17. ***b)*** *Khurutse fault scarp cross-sections with measured geomorphic offsets, in meters.*

7 Discussion

Although previous studies using teleseismic data and InSAR provided initial results on the 2017 Moiyabana earthquake, our investigations present the integration of near field and remote sensing studies including seismology, seismotectonic and Radar satellite images. Field investigations using six portable seismic stations supplemented with data from nearby permanent broadband seismic stations and tectonic geomorphology combined with the study of InSAR data, brought new insights in the study of the 2017 Moiyabana earthquake (M_W 6.5). Focal mechanism solutions indicate that the mainshock ruptured on a NW-SE trending blind normal fault. More than 900 aftershocks shed light on the fault rupture geometry within ~30 km depth of the Limpopo Mobile Belt in Botswana. Two aftershock sequences range between 5 and 30 km depth and show the complexity of the active crustal structure that delineates a NW-SE trending, and 20 to 30 km wide graben structure. Most of the aftershocks are of normal faulting mechanism with a general NE-SW extension direction confirmed by the stress tensor inversion.

Interferograms obtained from the analysis of Sentinel 1A images display 2 to 3 fringes (from which we infer 3.86 to 5.15 cm vertical displacement) that form two lobes coincident with the mainshock and aftershock locations. The modelling of coseismic rupture and slip distribution obtained from the inversion of surface deformation suggests ~40-km-long and ~22-km-wide fault geometry with the fault striking 315°, dipping 45°, with -80° rake, with two asperities and a maximum 50 cm slip distribution. This is different from Albano *et al.* (2017) InSAR inferred coseismic model of 20- km-long rupture plane, dipping 65° to the northeast, with a right-lateral component, and 2.7 m maximum slip at depth. In the absence of near field seismicity data and using InSAR results with a Bayesian estimate of source parameters, Gardonio *et al*. (2018) suggest both ~17° and ~73° dipping fault planes and a poorly estimated hypocentre depth of 29 ± 4 km. From the inversion of InSAR results coupled with geophysical (aeromagnetic and gravity) data, Kolawole *et al.* (2017) test several fault patches and estimate 21 to 24 km hypocentre depth on a 53° NE dipping fault plane, comparable with our 22 ± 1.5 km depth and 45° NE dipping fault plane.

7.1 Rifting propagation within intraplate southern Africa

Large intraplate earthquakes ($M_W \geq 6$) in southern Africa may result from complex continental tectonics and elastic strain release with continuum deformation rather than movements of rigid blocks (Scholz *et al.*, 1976; Reeves *et al.*, 2004). The rifting of the Ghanzi-Chobe Proterozoic Belt, due to the extensional forces during the Kibaran Orogeny, gave rise to the beginning of the Okavango rifting (Leseane *et al.*, 2015). This is the area where a significant seismic sequence occurred on 11 September 1952 with M_L 6.1 and another of M_L 6.7 on 11 October 1952. The Zoetfontein fault is another active zone in Botswana which has been known to be seismically active, thus revealing a background seismicity associated with long-term deformation and faulting (Dorland *et al.*, 2006). Its boundary with the Zimbabwe Craton is on the Limpopo-Shashe Thrust Zone (Ranganai *et al.*, 2002). The 2017 Moiyabana earthquake reveals the existence of a NW-SE trending active normal fault zone within the Limpopo Mobile Belt in Botswana. Daly *et al.* (2020) investigated the Okavango normal fault system using SRTM1" and Pleaides images and identified NE to ENE trending faults with evidence of vertical displacement. At a larger scale, normal faulting mechanisms of Moiyabana, Okavango and Machaze active zones reflect the complex crustal deformation within the Nubian Plate (Kinabo *et al.*, 2008; Fenton and Bommer 2006; Fonseca *et al.*, 2014). As compared to the region where the 2017 Moiyabana earthquake is located, the EARS is much more seismically active, since it is a divergent plate boundary. Furthermore, the 2017 Moiyabana earthquake and Okavango active zones with related seismotectonic framework appear as an extension of the EARS to the west (Kinabo *et al.*, 2008). Hence, the Limpopo Mobile Belt and Okavango active zones mark the possible development of new rifting zones within Nubia active plate interior.

7.2 Seismotectonics of intraplate earthquakes in southern Africa

A detailed analysis of the mainshock and aftershocks of the 2017 Moiyabana earthquake sequence in Botswana and related surface deformation lead to a better understanding of the intraplate seismic activity in southern Africa. The coseismic fault has been documented by means of the two seismic sequences that illustrate the rupture geometry at depth. The use of two different software packages (SEISAN and HypoDD) for the earthquake locations provides an insight to the seismic sequence at depth that illustrates the fault rupture geometry.

The coincidence in the location of mainshock, aftershocks, InSAR lobe results, and composite fault scarp reflects the long-term active deformation in the intraplate tectonic environment. Although the strain rate is rather low (~1 nanostrain/yr.), the occurrence of the 2017 Moiyabana earthquake constrains us to classify the Limpopo Mobile Belt as an active tectonic zone with a recurrent seismic strain release. These observations do not support the suggested hypothesis that the 2017 Moiyabana earthquake can be due to transient perturbations of local stresses due to pore fluid pressure (Gardonio *et al.*, 2018). The recurrence interval of large seismic events with surface deformation may reach several thousands of years that results from long-term but persistent seismic cycles (Camelbeeck and Meghraoui, 1998). In some regions such as Mongolia, major earthquakes in 1905 and 1957 with M_W 8 and 8.5, respectively, leave evidence of multiple rupture over the years (Chéry *et al.*, 2001). The study of recent earthquakes with near field investigations is crucial for a better understanding of the intraplate seismicity and active deformation in intraplate southern Africa.

8 Conclusion

The near field study of the 2017 Moiyabana earthquake (Mw 6.5) provides data and results on the crustal deformation of the intraplate tectonic domain of southern Africa. The detailed mainshock and aftershocks analysis shows a seismic sequence that suggests a fault-rupture geometry in agreement with normal focal mechanisms. The aftershocks analysis and focal mechanism solutions show predominately normal faulting that agrees with the NE-SW extensional stress regime in the region. Two distinct NW-SE to N-S trending aftershock sequences of more than 900 earthquakes processed using SEISAN, of which 699 aftershocks were relocated using the HypoDD program, are concentrated between 10 and 30 km depth. The distance between the two sequences being ~20 km, seismic events depict a graben-like structure where the mainshock and largest aftershock are located within the western sequence. The InSAR analysis shows the colocation of surface deformation with the western earthquake sequence and allows the modelling of a NW-SE trending fault rupture, dipping NE with an average 50 cm slip distribution and a seismic moment M_o 3.68 x 10^{18} Nm (Mw 6.4). SE of the epicentral area, we identified the NNW-SSE to NW-SE trending composite and sharp scarp morphology of the Khurutse fault scarp that aligns with the 2017 Moiyabana earthquake rupture. The active Okavango and Zoetfontein fault region, in the north and south of the Moiyabana earthquake location, respectively; indicate that the southern African continental region is active. In addition, the Khurutse fault scarp reflects a cumulative surface deformation, clearly highlighting the presence of a seismic cycle in this intraplate context.

Acknowledgements:

The work is supported by the Council of Geoscience (Pretoria), the Institut de la Terre et Environnement de Strasbourg (ITES) and UNESCO IGCP-659 project, and TM benefited from a Campus France scholarship of the French Embassy in Pretoria. The Council of Geoscience and Botswana Geoscience Institute provided field assistance for seismic stations deployment and for DGPS measurements of the Khurutse fault scarp. We are thankful to the European Space Agency for providing the Sentinel SAR images. We are indebted to Sophie Lambotte (ITE Strasbourg) for assistance in the relocation processing, Mohamed Khelif (CRAAG, Algiers) for assistance with SEISAN, Damien Delvaux for assistance with WinTensor program and Klaus Hinzen (University of Cologne) for discussion on an earlier version of manuscript. All figures have been produced using Generic Mapping Tools (Wessel & Smith 1998). We are also thankful to the Editor Mohamed G Abdelsalam and reviewer Sarah Stamps for their comments that improve the presentation of our manuscript.

References

Albano, M., Polcari, M., Bignami, C., Moro, M., Saroli, M., Stramondo, S., 2017. Did Anthropogenic Activities Trigger the 3 April 2017 Mw 6.5 Botswana Earthquake?, Remote Sens., 9 (10), 1028 – 1040.

Andreoli, M. A. G., Doucoure, M., Van Bever Donker, J., Brandt, D., Andersen, N. J. B., 1996. Neotectonics of southern Africa: A review, Afr. Geosci. Rev., 3(1), 1–16.

Angelier, J. Mechler, P., 1977. Sur une méthode graphique de recherche des contraintes principales également utilisable en tectonique et en séismologie: la méthode des dièdres droits, Bull. Soc. géol. Fr., 19, 1309 – 1318.

Begg, G. C., Griffin, W. L., Natapov, L. M., O'Reilly, S. Y., Grand, S. P., O'Neill, C. J., Hronsky, J. M. A., Poudjom Djomani, Y., Swain, C.J., Deen, T., Bowden, P., 2009. The Lithospheric Architecture of Africa: Seismic Tomography, Mantle Petrology, and Tectonic Evolution, Geosphere, 5, 23 – 50.

Bent, A. L., 1994. The 1989 (Ms 6.3) Ungava, Quebec, earthquake: A complex intraplate event, Bull. Seismol. Soc. Am., 84(4), 1075 – 1088.

Brown, R., Gernon, T., Stiefenhofer, J., Field, M., 2008. Geological constraints on the eruption of the Jwaneng Centre kimberlite pipe, Botswana. J. Volcanol. Geotherm. Res., 174 (1), 195 – 208.

Burbank, D. W., Anderson, R. S., 2001. Tectonic geomorphology, Blackwell Science Ltd, Oxford, United Kingdom.

Calais, E., T. Camelbeeck, Stein, S., Liu, M., Craig, T. J., 2016. A new paradigm for large earthquakes in stable continental plate interiors, Geophys. Res. Lett, 43(20), 10621 – 10637.

Camelbeeck, T., Meghraoui, M., 1998. Geological and geophysical evidence for large paleoearthquakes with surface faulting in the Roer Graben (northwest Europe), Geophys. J. Int., 132, 347 – 362.

Chéry, J., Carretier, S., Ritz, J.-F., 2001. Postseismic stress transfer explains time clustering of large earthquakes in Mongolia, Earth Planet. Sci. Lett., 194(1–2), 277–286, doi:10.1016/S0012-821X(01)00552-0.

Chisenga, C., Van der Meijde, M., Yan, J., Fadel, I., Atekwana, E. A., Steffen, R., Ramotoroko, C., 2020. Gravity derived crustal thickness model of Botswana: Its implication for the Mw 6.5 April 3, 2017, Botswana earthquake, Tectonophysics, 787. https://doi.org/10.1016/j.tecto.2020.228479

Clark, D., Dentith, M., Wyrwoll, K. H., Yanchoul, L., Dent, V., Featherstone, C., 2008. The Hyden fault scarp, Western Australia: paleoseismic evidence for repeated Quaternary displacement in an intracratonic setting, Aust. J. Earth Sci., 55, 379 – 395.

Crone, A. J., Machette, M. N., Bowman, J. R., 1997. Episodic nature of earthquake activity in stable continental regions revealed by palaeoseismicity studies of Australian and North American quaternary faults, Aust. J. Earth Sci., 44(2), 203–214.

Daly, M. C., Green, P., Watts, A. B., Davies, O., Chibesakunda, F., Walker, R., 2020. Tectonics and landscape of the Central African Plateau and their implications for a propagating Southwestern Rift in Africa, Geochemistry, Geophys. Geosystems, 21, 1 – 37, doi.org/10.1029/2019GC008746.

Delvaux, D., 1993. The TENSOR program for paleostress reconstruction: examples from the east African and the Baikal rift zones. EUG VII Strasbourg, France, 4–8 April 1993. Abstract supplement N°1 to Terra Nov. 5: 216.

Delvaux, D. B., Sperner, 2003. New aspects of tectonic stress inversion with reference to the TENSOR program. In: New Insights into Structural Interpretation and Modelling (D. Nieuwland Ed.). Geological Society, London, Special Publications 212: 75 – 100.

Delvaux, D., Barth, A., 2010. African stress pattern from formal inversion of focal mechanism data. Implications for rifting dynamics, Tectonophysics, 482, 105 – 128.

Dorland, H. C., Beukes, N. J., Gutzmer, J., Evans, D. A. D., Armstrong, R. A., 2006. Precise SHRIMP U-Pb zircon age constraints on the lower Waterberg and Soutpansberg Groups, South Africa, S Afr J Geol, 109, 139 – 156.

Fadel, I., Paulssen, H., van der Meijde, M., Kwadiba, M., Ntibinyane, O., Nyblade, A., Durrheim, R., 2020. Crustal and Upper Mantle Shear Wave Velocity Structure of Botswana: The 3 April 2017 Central Botswana Earthquake Linked to the East African Rift System, Geophys. Res. Lett, 47(4).

Farr, T. G., Rosen, P. A., Caro, E., Crippen, R., Duren, R., Hensley, S., Kobrick, M., Paller, M., Rodriguez, E., Roth, L., Seal, D., Shaffer, S., Shimada, J., Umland, J., Werner, M., Oskin, M., Burbank, D., Alsdorf, D., 2007. The Shuttle Radar Topography Mission, Rev. Geophys., 45, RG2004, doi:10.1029/2005RG000183.

Fairhead, J., Henderson, N., 1977. The seismicity of Southern Africa and incipient rifting, Tectonophysics, 41, 19–26.

Fenton, C., Bommer, J., 2006. The M_W 7 Machaze, Mozambique, earthquake of 23 February 2006, Seism. Res. Lett., 77, 426–439, doi:10.1785/gssrl.77.4.426.

Fonseca, J.F.B.D., Chamussa, J., Domingues, A., Helffrich, G., Antunes, E., van Aswegen, G., Pinto, L.V., Cust_odio, S., Manhiça, V.J., 2014. MOZART: a seismological investigation of the east African rift in Central Mozambique. Seismol Res. Lett. 85 (1), 108 – 116.

Fourie, C. J. S., Henry, G., Maré, L. P., 2014. The structure of the Karoo-age Ellisras Basin in Limpopo Province, South Africa in the light of new airborne geophysical data: a preliminary report, S Afr J Geol, 117 (2), 207 – 224.

Gardonio, B., Jolivet, R., Calais, E., Leclère, H., 2018. The April 2017 Mw6.5 Botswana Earthquake: An Intraplate Event Triggered by Deep Fluids, Geophys. Res. Lett, 45 (17), 8886 – 8896.

Hartnady, C., 1990. Seismicity and plate boundary evolution in Southeastern Africa, S. Afr. J. Geol., 93, 473–484.

Hough, S. E., Page, M., 2011. Toward a consistent model for strain accrual and release for the New Madrid Seismic Zone, central United States, J. Geophys. Res., 116, B03311, doi:10.1029/2010JB007783.

Johnston, A.C., 1996a. Seismic moment assessment of earthquakes in stable continental regions—I. Instrumental seismicity, Geophys. J. Int., 124 (2), 381– 414.

Johnston, A.C., 1996b. Seismic moment assessment of earthquakes in stable continental regions—II. Historical seismicity, Geophys. J. Int., 125 (3), 639 – 678.

Kinabo, B., Hogan, J., Atekwana, E., Abdel Salam, M. Modisi, M., 2008. Fault growth and propagation during incipient continental rifting: inside from a combined aeromagnetic and Shuttle Radar Topography Mission digital elevation model investigation of the Okavango Rift Zone, northwest Botswana, Tectonics, 27, doi:10.1029/2007TC002154.

Kolawole, F., Atekwana, E. A., Malloy, S., Stamps, D. S., Grandin, R., Abdelsalam, M. G., Leseane, K., Shemang E. M., 2017. Aeromagnetic, gravity, and Differential Interferometric Synthetic Aperture Radar (DInSAR) analyses reveal the causative fault of the 3 April 2017 Mw 6.5 Moiyabana, Botswana Earthquake, Geophys. Res. Lett, 44, 8837 – 8846.

Lekula, M., Lubczynskia, M. W., Shemang, E. M., 2018. Hydrogeological conceptual model of large and complex sedimentary aquifer systems – Central Kalahari Basin, Phys Chem Earth, 106, 47 – 62.

Leseane, K., Atekwana, E. A., Mickus, K. L., Abdelsalam, M. G., Shemang E. M., Atekwana, E. A., 2015. Thermal perturbations beneath the incipient Okavango Rift Zone, northwest Botswana, J. Geophys. Res. Solid Earth, 120 (2), 1210 – 1228.

Lienert, B. R., Berg, E., Frazer, L. N., 1986. Hypocenter: an earthquake location method using centered, scaled, and adaptively damped least squares, Bull. Seismol. Soc. Am., 76(3), 771 – 783.

Lienert, B. R., Havskov, J., 1995. A Computer Program for Locating Earthquakes Both Locally and Globally, Seismol. Res. Lett., 66 (5), 26 – 36.

Malservisi, R., Hugentobler, U., Wonnacott, R., Hackl, M., 2013. How rigid is a rigid plate? Geodetic constraint from the TrigNet CGPS network, South Africa, Geophys. J. Int., 192, 918 – 928.

Manzunzu, B., Midzi, V., Mangongolo, A., Essrich, F., 2017. The aftershock sequence of the 5 August 2014 Orkney earthquake (ML 5.5), South Africa, J. Seismol., 21, 1323 – 1334.

Maerten, F., Resor, P., Pollard, D., Maerten, L., 2005. Inverting for slip on three-dimensional fault surfaces using angular dislocations, Bull. Seismol. Soc. Am., 95 (5), 1654 – 1665.

Materna, K., Wei, S., Wang, X., Heng, L., Wang, T., Chen, W., Salman, R., Bürgmann, R., 2019. Source characteristics of the 2017 Mw6.4 Moijabana, Botswana earthquake, a rare lower-crustal event within an ancient zone of weakness, Earth Planet Sci Lett, 506, 348 – 359.

Meghraoui, M., Amponsah, P., Ayadi, A., Ayele, A., Ateba, B., Bensuleman, A., Delvaux, D., El Gabry, M., Fernandes, R., 2016. The Seismotectonic Map of Africa, Episodes, 39 (1), 9 – 18.

Midzi, V., Saunders, I., Brandt, M. B. C., Molea, T., 2010. 1-D velocity model for use by the SANSN in earthquake location, Seismol. Res. Lett., 81 (3), 460 – 466.

Midzi, V., Saunders, I., Manzunzu, B., Kwadiba, M. T., Jele, V., Mantsha, R., Marimira, K. T., Mulabisana, T. F., Ntibinyane, O., Pule, T., Rathod, G. W., Sitali, M., Tabane, L., van Aswegen, G., Zulu, B. S., 2018. The 03 April 2017 Botswana M6.5 earthquake: Preliminary results, J. African Earth Sci., 143, 187 – 194.

Modisi, M., Atekwana, E., Kampunzu, A., Ngwisanyi, 2000. Rift kinematics during the incipient stages of continental extension: evidence from the nascent Okavango Rift basin, northwest Botswana, Geology, 28, 939–942.

Moorkamp, M., Fishwick, S., Walker, R. J., Jones, A. G., 2019. Geophysical evidence for crustal and mantle weak zones controlling intra-plate seismicity – the 2017 Botswana earthquake sequence, Earth Planet Sci Lett, 506, 175 – 183.

Nguuri, T. K., Goree, J., James, D. E., Webb, S. J., Wright, C., Zengen, T. G., Gwavava, O., Snoke, J., A Kaapvaal Seismic Group, 2001. Crustal structure beneath southern Africa and its implications for the formation and evolution of the Kaapvaal and Zimbabwe cratons, Geophys. Res. Letters 28, 13, 2501-2504.

Njoroge, M., R. Malservisi, Voytenko, D., Hackl, M., 2015. Is Nubia Plate Rigid? A geodetic study of the relative motion of different cratonic areas within Africa, International Association of Geodesy Symposia, p 1-9, doi:10.1007/1345_2015_212

Okada, Y., 1985. Surface deformation due to shear and tensile faults in a half-space, Bull. Seismol. Soc. Am., 75 (4), 1135 – 1154.

Olebetse, T.A., Mmese, M.L., Simon, R.E., Maritinkole, J., 2020. Some Foreshocks and Aftershocks Associated with the Moiyabana Earthquake of 2017 in Botswana. Int. J. Geosci., 11, 238-250. https://doi.org/10.4236/ijg.2020.114013

Ottemöller, L., Voss, P., Havskov, J., 2018. SEISAN Earthquake Analysis Software for Windows, Solaris, Linux and Macosx. Bergen.

Rajendran, C. P., Rajendran, K., John, B., 1996. The 1993 Killari (Latur), central India, earthquake: An example of fault reactivation in the Precambrian crust, Geology 24, 651–654.

Ranganai, R. T., Kampunzu, A. B., Atekwana, E. A., Paya, B. K., King, J. G., Koosimile, D. I., Stettler, E. H., 2002. Gravity evidence for a larger Limpopo Belt in southern Africa and geodynamic implications, Geophys J Int., 149 (3), F9 – F14.

Reeves, C., de Wit, M. Sahu, B., 2004. Tight reassembly of Gondwana exposes phanerozoic shears in Africa as global tectonic players, Gondwana Res., 7, 7–19.

Roering, C., van Reenen, D. D., Smit, C. A., Barton, J. M., de Beer, J. H., de Wit, M. J., Stettler, E. H., van Schalkwyk, J. F., Stevens, G., Pretorius, S., 1992. Tectonic model for the evolution of the Limpopo Belt, Precambrian Res., 55, 539 – 552.

Ross, Z. E., Meier, M., Hauksson, E., 2018. P wave arrival picking and first-motion polarity determination with deep learning, J. Geophys. Res. Solid Earth, 123 (6), 5120 – 5129.

Sandwell, D., Mellors, R., Tong, X., Wei, M., Wessel, P., 2011. GMTSAR: An InSAR Processing System Based on Generic Mapping Tools. UC San Diego: Scripps Institution of Oceanography. Retrieved from: http://escholarship.org/uc/item/8zq2c02m.

Saria, E., Calais, E., Stamps, D.S., Delvaux, S. Hartnady, C.J.H., 2014. Present-day kinematics of the East African Rift, J. geophys. Res., 119, doi:10.1002/2013JB010901.

Saunders, I., Brandt, M.B.C., Molea, T.T., Akromah, L. Sutherland, B., 2010. Seismicity of Southern Africa during 2006 with special reference to the Mw 7 Machaze earthquake. S Afr J Geol, 113, 4, 369-380.

Scholz, C., Kocynski, T. Hutchins, D., 1976. Evidence for incipient rifting in Southern Africa, Geophys. J. R. astr. Soc., 44, 135–144.

Stamps, D. S., Flesch, L. M., Calais, E., Ghosh, A., 2014. Current kinematics and dynamics of Africa and the East African Rift System, J. Geophys. Res. Solid Earth, 119, 5161 – 5186, doi:10.1002/2013JB010717.

Stamps, D. S., Saria, E., Kreemer, C., 2018. A Geodetic Strain Rate Model for the East African Rift System, Sci. Rep., 8(1), 1 – 8.

Thomas, A., 2020. Mapping of Surface Deformation and Displacement Associated with the 6.5 Magnitude Botswana Earthquake of 3 April 2017 Using DInSAR Analysis, Geomat. Environ. Eng., 14, 4, https://doi.org/10.7494/geom.2020.14.4.81

Utsu T., Ogata, Y., Matsu'ura ; R.S., 1995. The centenary of the Omori formula for a decay law of aftershock activity, J. Phys. Earth, 43, 1-33.

Waldhauser, F., Ellsworth, W. L., 2000. A Double-Difference Earthquake Location Algorithm: Method and Application to the Northern Hayward Fault, California, Bull. Seismol. Soc. Am., 90 (6), 1353 – 1368.

Waldhauser, F., 2001. HypoDD: A computer program to compute double-difference earthquake locations, USGS Open File Rep., 01-113.

Wessel, P., Smith, H.F., 1998. New, improved version of the generic mapping tools released. EOS Trans. AGU 79, 579.

Williamson, I. T., 1996. The geology of the areas around Mmamabula and Dibete: including an account of the Greater Mmamabula Coalfield, Geological Survey Department: District Memoir 6, Chapter 1, pp 03.

Zoback, M. L., Zoback, M. D., 1989. Tectonic stress field of the continental United States: In Geological Society of America Memoir 172, Chapter 24, 523 – 539.

Tables

Seismological Centre	Long. (°)	Lat. (°)	M_0 (Nm)	M_w	Depth (km)	Strike	Dip	Rake
USGS (Wpha)	25.15	-22.678	$6.19\ 10^{18}$	6.5	23.5	343	44	-62
GFZ	25.22	-22.66	$6.3\ 10^{18}$	6.5	27	331	37	-73
Geoscope	25.15	-22.678	$5.86\ 10^{18}$	6.4	29	333	36	-72
CMT Harvard	25.21	-22.54	$7.01\ 10^{18}$	6.5	30	332	41	-70
CGS (Pretoria) Midzi et al. (2018)	25.134	-22.565	-	6.5	26.5 ±2.5	340	46	-61
This study (InSAR)	25.134	-22.565	$3.68\ 10^{18}$	6.4	22 ±1.5	315	45	-80

***Table 3**: Source parameters of the 3 April 2017 earthquake.*

Modified depth to top of layer (km)	**P-wave velocity (km/s)**
0.00	5.80
20.00	6.50

38.00	8.04

***Table 2**: Velocity model (Midzi et al., 2010) used in initial location of aftershocks using Seisan software as well as in the double difference relocation using the hypoDD software.*

Table Captions

Table 4: Source parameters of the 3 April 2017 earthquake.

Table 2: Velocity model (Midzi et al., 2010) used in initial location of aftershocks using Seisan software as well as in the double difference relocation using the hypoDD software.

Supporting Information

Supplementary Material:

- SM1: Table of Focal Mechanisms of Fig. 1.
- SM2: Spatial distribution and cross section of aftershock locations before and after the 8th of April 2017 (installation of temporary network).
- SM3: Spatial distribution of aftershock locations before and after DD relocation.
- SM4: Table of list of aftershocks and focal mechanisms.
- SM5: InSAR processing and modelling.

Resources

- Topography GEBCO: https://www.gebco.net/data_and_products/gridded_bathymetry_data/
- Topography SRTM 3" and 1": https://topex.ucsd.edu/gmtsar/demgen/
- Database of the Seismotectonic Map of Africa: Meghraoui et al., 2016

- ESA Sentinel images : https://sentinel.esa.int/web/sentinel/sentinel-data-access
- SEISAN package : ftp://ftp.geo.uib.no/pub/seismo/SOFTWARE/SEISAN/
- HypoDD: https://www.ldeo.columbia.edu/~felixw/hypoDD.html
- WinTensor software: http://damiendelvaux.be/Tensor/WinTensor/win-tensor_download.html

- A study of the 2017 Botswana aftershock sequence in a continental interior.
- The fault geometry from aftershocks analysis, InSAR and tectonic geomorphology.
- Understanding earthquake generation processes using near-field seismology.
- Possible development of new rifting zones within Nubia continental domain.

Declaration of interests

☒ The authors declare that they have no known competing financial interests or personal relationships that could have appeared to influence the work reported in this paper.

☐The authors declare the following financial interests/personal relationships which may be considered as potential competing interests: